# Fabrication of Superconducting Nanowire Single Photon Detectors

by

Joel K. Yang

Submitted to the Department of Electrical Engineering and Computer Science
in partial fulfillment of the requirements for the degree of

Master of Science in Electrical Engineering and Computer Science

at the

MASSACHUSETTS INSTITUTE OF TECHNOLOGY

July 2005

© Massachusetts Institute of Technology 2005. All rights reserved.

Author ....................................
Department of Electrical Engineering and Computer Science
July, 2005

Certified by ..................
Karl K. Berggren
Assistant Professor of Electrical Engineering and Computer Science
s Supervisor

Accepted by ............
Arthur C. Smith
Chairman, Department Committee on Graduate Students

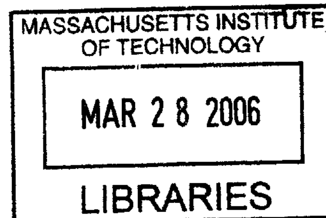


BARKER

# Fabrication of Superconducting Nanowire Single Photon Detectors

by

Joel K. Yang

Submitted to the Department of Electrical Engineering and Computer Science
on July, 2005, in partial fulfillment of the
requirements for the degree of
Master of Science in Electrical Engineering and Computer Science

## Abstract

The future NASA Mars project will need an ultra-fast, highly sensitive photodetector to increase the bandwidth of free-space long-range communication, which is now done primarily using RF signals. Our original motivation in fabricating superconducting nanowire single-photon detectors (SN-SPD) is to fulfil this need. The SN-SPD's reported GHz counting rates [1] make it very attractive for this application. A new fabrication process for making SN-SPDs using hydrogen-silsesqioxane (HSQ), a high-resolution electron-beam lithography resist will be presented. An electron-beam proximity-effect correction program was developed to achieve nanowires with uniform linewidths, which is important for device performance. Finally, we present initial test results that show device functionality and performance. Our best device has a detection efficiency of $\sim$ 10 % at 1064 nm photon wavelength at 2.1 K and a photon-induced voltage-pulse duration of $\sim$ 3 ns.

Thesis Supervisor: Karl K. Berggren
Title: Assistant Professor of Electrical Engineering and Computer Science

## Acknowledgments

This project would not have been possible without the constant guidance, advice and enthusiasm from my advisor, Professor Karl K. Berggren. I am thankful to him for creating a nurturing environment where I can develop my scientific skills.

I am also indebted to a multitude of people who have contributed to this project in different ways.

To Professor Henry Smith for his expertise in nanofabrication.

To Rajesh Menon, for introducing me to Professor Karl Berggren and Professor Henry Smith.

To Eric Dauler and Andrew Kerman of Lincoln Laboratory for sharing many exciting discoveries during this project.

To Professor Rajeev Ram and Professor Terry Orlando for their generosity in allowing me to use their laboratories.

To Mark Mondol, Feng Zhang and Tymon Barwicz for their excellent technical knowledge on the Raith 150.

To Jim Daley for making things possible in the NanoStructures Laboratory.

To my group mates, past and present, Antonin Ferri, Bryan Cord, Delano Sanchez, Kristine Rosfjord, Ma Yunjie, Magnus Rådmark, Nicolas Boulant, Stefan Harrer, and Vikas Anant, for their friendship and for sweetening the working experience.

To the folks at NIST, Robert Hadfield, Aaron Miller, Saw Woo Nam, Robert Schwall, for an exciting collaboration and thoughtful discussions.

To our collaborators, Gregory Gol'tsman, Roman Sobolewski and Alexander Verevkin for starting us off in the right direction.

To Minghao Qi, Fernando Castaño, David Chao, Euclid Moon, Tim Savas and all the other members of the NanoStructures Laboratory, for sharing the "nano" experience.

To Jonathan Habif and Matthew Abraham for their help in handling cryogenic equipment.

To my sponsor in Singapore, Agency for Science Technology and Research (A*STAR)

for giving me the opportunity to study at MIT.

To my family in Singapore, Malaysia and Indonesia, for always believing in me.

Above all, to my loving wife, Ariani, for her strength and support. I owe all my happiness to you. Thank you for always being here with me as we share an amazing life together.

# Contents


**1 Introduction** **15**

1.1 Previous work on superconducting nanowire single photon detectors (SN-SPDs) . . . 16

1.2 Applications of single photon detectors (SPD) . . . 17

1.3 Principle of operation of the SN-SPD . . . 18

1.4 Description of the SN-SPD . . . 19

1.5 Requirements for nanowire dimensions and smoothness . . . 19

1.6 Objectives and challenges . . . 22

1.7 Summary of work done in this project . . . 22

**2 Defining gold contact pads** **25**

2.1 Liftoff process . . . 26

2.2 Challenges in liftoff for small samples . . . 27

2.3 Contact printing photolithography . . . 28

2.3.1 Ideal contact printing photolithography and effect of edge beads 28

2.4 Process details . . . 29

2.4.1 Resist spin coating . . . 30

2.4.2 Contact photolithography . . . 31

2.4.3 Creating an overhang structure . . . 32

2.4.4 Photoresist development . . . 33

2.4.5 Metal deposition by electron-beam evaporation . . . 33

2.4.6 Heating effects of metal deposition . . . 33

2.4.7 Final liftoff step . . . 35

2.5 Summary . . . 35

**3 Patterning nanowires in NbN** **37**

3.1 Electron-beam lithography . . . 37

3.2 Proximity effects in EBL . . . 38

3.3 Modeling the electron beam . . . 40

3.4 Proximity-effect correction . . . 41

3.5 Experimental results . . . 45

3.5.1 Quantitative measurement of linewidth variation . . . 45

3.6 Determining the accuracy of the PEC . . . 46

3.7 Designing arbitrary meanders . . . 48

3.8 Hydrogen-Silsesquioxane (HSQ) negative-tone electron resist . . . 49

3.8.1 Background information on HSQ . . . 49

3.8.2 HSQ exposure mechanism . . . 50

3.8.3 HSQ development mechanism . . . 53

3.8.4 Process details, experiments and results . . . 53

3.8.5 HSQ contrast . . . 55

3.8.6 Adhesion problems . . . 57

3.8.7 HSQ and NbN wettability experiments . . . 57

3.8.8 Solving adhesion problems . . . 58

3.9 Reactive ion etching . . . 59

3.10 Material damage . . . 61

3.10.1 Plasma-induced damage . . . 61

3.10.2 Thermal damage . . . 62

3.10.3 Chemical damage . . . 62

3.11 Summary . . . 63

**4 Electrical and optical testing of SN-SPDs** **65**

4.1 Cryogenic DC measurements . . . 65

4.1.1 Experimental setup . . . 65

4.2 DC measurement results . . . 66

4.2.1 $I$-$V$ characteristics . . . . . . . . . . . . . . . . . . . . . . 67
4.2.2 Problems with electrical contact during DC measurements . . 67
4.2.3 $I_c$ dependence on temperature . . . . . . . . . . . . . . . . . 68
4.2.4 Resistance temperature dependence . . . . . . . . . . . . . . . 69
4.2.5 $I_c$ and conductivity dependence on wire width . . . . . . . . . 69
4.3 High-speed tests . . . . . . . . . . . . . . . . . . . . . . . . . . 70
4.3.1 Experimental setup . . . . . . . . . . . . . . . . . . . . . . . 70
4.3.2 High-speed test results . . . . . . . . . . . . . . . . . . . . . 72
4.3.3 Single-photon detection . . . . . . . . . . . . . . . . . . . . . 73
4.4 Device modeling . . . . . . . . . . . . . . . . . . . . . . . . . . 76
4.4.1 Hotspot model . . . . . . . . . . . . . . . . . . . . . . . . . 76
4.4.2 Kinetic inductance of SN-SPD . . . . . . . . . . . . . . . . . . 77
4.5 Future work . . . . . . . . . . . . . . . . . . . . . . . . . . . . 80

# List of Figures

1-1 SN-SPD detection mechanism. . . . . . . . . . . . . . . . . . . . . . . . 18
1-2 (Left) Scanning electron micrograph (SEM) image of a patterned electron beam resist on NbN film. (Right) SEM image of a zoomed in view of the meander. The active area consists of 90 nm wide nanowires folded tightly in a meander structure. . . . . . . . . . . . . . . . . . . . 20
1-3 A schematic drawing of a nanowire with a severe constriction where the current density is highest. . . . . . . . . . . . . . . . . . . . . . . . 20
1-4 Process flow for fabricating SN-SPD. . . . . . . . . . . . . . . . . . . . 23

2-1 Diagram of a coplanar waveguide (CPW) connected to the SN-SPD. 26
2-2 Process flow for liftoff. . . . . . . . . . . . . . . . . . . . . . . . . . . 27
2-3 Sloped sidewalls cause problematic liftoff. . . . . . . . . . . . . . . . . 28
2-4 a) Ideal contact photolithography setup. b)Case when edge beads are present. . . . . . . . . . . . . . . . . . . . . . . . . . . . . . . . . . . 29
2-5 Relationship among exposure dose, resist contrast, development time and resultant resist profile. . . . . . . . . . . . . . . . . . . . . . . . . 30
2-6 Spin curve for Shipley Microposit S1813. . . . . . . . . . . . . . . . . 31
2-7 SEM image of overhang structures in S1813 photoresist on silicon created by immersion in chlorobenzene prior to developemnt. . . . . . . 32
2-8 SEM image of an overhang structure after 10 nm of Ti and 50 nm of Au have been deposited by electron-beam evaporation. . . . . . . . . 35

3-1 An illustration of forward and backward scattering of the electron beam during exposure. . . . . . . . . . . . . . . . . . . . . . . . . . . . . 38

3-2 SEM image showing one corner of a 200 nm period grating written in HSQ at 10 kV using the Raith 150 EBL. . . . . . . . . . . . . . . . . . 39
3-3 Layout of the meander design as it appears in a GDS2 file editor. . . 43
3-4 Matlab simulation plots of areal dose (shown using different colors) at every position of the meander pattern. . . . . . . . . . . . . . . . . . 44
3-5 SEM image of meander patterns written in HSQ before (a) and after (b) the PEC program was developed and used. . . . . . . . . . . . . . 45
3-6 Plot of measured linewidth at strategic locations on the resultant meander for two cases. . . . . . . . . . . . . . . . . . . . . . . . . . . 46
3-7 SEM image showing one corner of the meander pattern where footing begins to appear with increasing dose. . . . . . . . . . . . . . . . . . 47
3-8 Plot of normalized linewidth versus dose in between lines for different meander designs . . . . . . . . . . . . . . . . . . . . . . . . . . . . 48
3-9 SEM image of two different meander designs using the PEC program. 49
3-10 Three dimensional cage-like molecular structure of HSQ. . . . . . . . 50
3-11 Schematic drawing illustrating a likely process that occurs during crosslinking. . . . . . . . . . . . . . . . . . . . . . . . . . . . . . . . . . 51
3-12 FTIR absorption spectra of a) unexposed HSQ resist and b) e-beam exposed HSQ resist. . . . . . . . . . . . . . . . . . . . . . . . . . . . 52
3-13 Cartoon drawing showing the possible reactions that occur during HSQ development. . . . . . . . . . . . . . . . . . . . . . . . . . . . . . 54
3-14 SEM images of gratings written using magnification range 1 (figure a) and magnification range 2 (figure b) settings on the Raith 150. . . . . 55
3-15 Contrast curve for 90 nm thick HSQ written at 30 kV and 4 nm step size using different concentration of developers. . . . . . . . . . . . . 56
3-16 SEM image showing HSQ structures that have peeled off the NbN surface and shifted from its original position after development. . . . 57
3-17 SEM image of a meander pattern after RIE. . . . . . . . . . . . . . . 60
3-18 SEM image of a damaged meander pattern after RIE. . . . . . . . . . 61

3-19 SEM image of a meander pattern with plasma induced explosion marks at the four corners. . . . . 62

4-1 Plot of V vs I for a 100 nm nanowire at different temperatures. . . . . 67
4-2 Plot of $I_c$ vs T for a 100 nm nanowire. . . . . 68
4-3 Plot of R vs T for a 100 nm nanowire. . . . . 69
4-4 A plot of $I_c$ versus wire width. All wires were 5 $\mu$m long. . . . . 70
4-5 A plot conductivity versus wire width. All wires were 5 $\mu$m long. . . . . 71
4-6 Circuit schematic for high-speed experimental setup. . . . . 72
4-7 Voltage pulse measured at the high speed oscilloscope of the SN-SPD response to an absorbed single photon. . . . . 72
4-8 Plot of detection efficiency for single photons against bias current for photon wavelengths of 1064 nm and 1550 nm and temperatures of 2.1 K and 4.22 K. . . . . 73
4-9 Plot of detector counts per second vs laser power. . . . . 74
4-10 Matlab plot of quasiparticle concentration at a point 20 nm from photon absorption. . . . . 77
4-11 Matlab plot of quasiparticle concentration 4 ps after photon absorption. The hotspot size is in the order of several tens of nm. . . . . 77
4-12 Schematic drawing showing an electrical model of the SN-SPD . . . . 79

# Chapter 1

# Introduction

The superconducting nanowire single photon detector (SN-SPD) is a particular type of single-photon detector (SPD) capable of detecting photons with energies as low as 0.8 eV (i.e. near-infrared wavelengths). This report will detail a new process for fabricating SN-SPDs and explain electrical measurements that verify device functionality.

Invented in 2001, SN-SPDs are new and are not the only available single photon detecting device. A list of several other types of SPDs are:

1. Photomultiplier tubes (PMT) [2]
2. Semiconductor avalanche photo-diodes (APD) [3]
3. Superconductor tunnel-junction detectors (STJ) [4]
4. Transition-edge sensors (TES) [5]
5. Superconducting kinetic inductance detectors (KID) [6]

Each detector type has a different principle of operation and different limitations. Some important SPD performance measures are listed below:

1. *Detection efficiency* (DE) - a measure of the probability of detecting an incident photon. DE values as close to unity as possible is desirable.

2. *Photon counting rates* - the maximum number of non-simultaneous photons that can be detected per unit time. GHz or even THz counting rates are desirable.

3. *Photon energy resolving capability* - the ability of the detector to measure the energy of an absorbed photon.

4. *Dark counts* - a measure of the frequency of false counts in the absence of any photons.

5. *Jitter* - a measure of the accuracy in which the SPD can determine the time of arrival of a photon.

SN-SPD is attractive due to its ultrafast photoresponse, low dark counts, and low jitter. It is the fastest SPD to date with counting rates orders of magnitude higher than other types of detectors [1] at infrared wavelengths.

## 1.1 Previous work on superconducting nanowire single photon detectors (SN-SPDs)

The principle of operation of the SN-SPD is based on the "hotspot" model in thin superconducting films, discovered by Kadin and Johnson in 1996 [7]. In 2001, Gol'tsman et al. developed a single photon detector based on this principle [8]. Some improvements in fabrication and testing techniques have been made since then with latest reported results of DE as high as $\sim 5$ % and $\sim 10$ % for 1550 nm and 1300 nm wavelengths respectively [9, 1]. Most impressively, the SN-SPD reportedly has a counting rate of 2 GHz [1], jitter of 18 ps and dark count of $< 0.01$ %. However, work is still needed to increase the SN-SPD DE before SN-SPDs can be used in most practical applications. Similarly, the SN-SPD has poor (or no) photon energy resolving capability as reported by Semenov in [10]. However, it is interesting to explore ways to improve this.

## 1.2 Applications of single photon detectors (SPD)

A wide range of applications for SPDs exists in different fields. In astronomical imaging, for example, SPDs are needed to detect weak electromagnetic radiation from distant astronomical objects. The SN-SPD is particularly well suited for applications that require high speed SPDs. These applications are listed below:

1. Laser communication link between Earth and Mars

2. Quantum cryptography or quantum key distribution

3. High speed non-contact testing of VLSI CMOS circuits

NASA is currently working to establish the first interplanetary laser communication link between Earth and Mars and hopes to test it by the end of the decade [11]. A collaboration of NASA's Goddard Space Flight Center, the Jet Propulsion Laboratory and MIT's Lincoln Laboratory is working to increase data communication rates using this laser link. The SN-SPD is a likely candidate as the next-next generation detector in this program with the promise of boosting the data communication rates up to hundreds of MHz.

Quantum key distribution (QKD), proposed by Bennett and Brassard in 1984, is a technique for sharing an assuredly secret, cryptographic key over unsecured optical links [12]. In QKD, information is encoded in the quantum state of individual photons, and security is guaranteed by the photons' fundamental quantum properties. A key component in QKD is the SPD. Using the SN-SPD may increase the speed of information transmission.

High speed testing of low-voltage VLSI chips is one application where SN-SPDs are already being used at IBM [13]. This technique for testing VLSI chips is called Picosecond Imaging Circuit Analysis (PICA). SN-SPDs provide a reduction in acquisition time of this technique by six orders of magnitude compared to photomultiplier tubes [13, 14].

## 1.3 Principle of operation of the SN-SPD

The SN-SPD is based on the formation of a resistive barrier across a narrow superconducting wire when a photon is absorbed. A superconductor exhibits zero DC electrical resistance when cooled down below its critical temperature, $T_c$.

The charge carriers in the resistive state of the material are electrons (often referred to as quasiparticles in superconductivity). In the superconducting state, charge carriers are Cooper pairs that are able to flow without resistance through the material crystal lattice. Cooper pairs form due to a lattice mediated net attractive force between two quasiparticles.

Every superconducting material has a characteristic $T_c$ and a critical current density, $j_c$. Therefore, in a narrow superconducting wire with cross sectional area of $A$, the supercurrent flows only up to a certain point called the critical current, $I_c = j_c A$. Above $I_c$, the wire switches into its resistive (or normal) state.

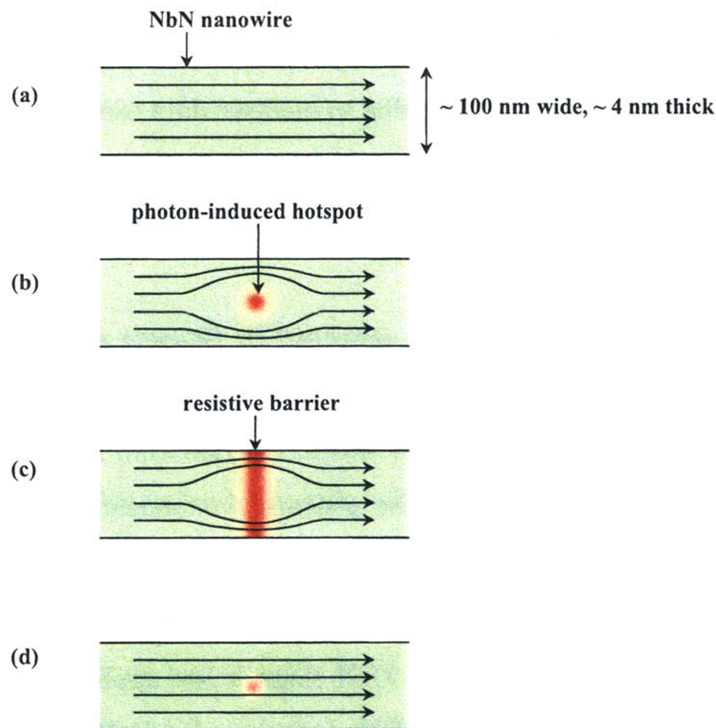


Figure 1-1: SN-SPD detection mechanism.

As illustrated in figure 1-1, the SN-SPD detection mechanism is as follows: (a)

A bias current, $I_b \lesssim I_c$ is passed through a narrow superconducting niobium-nitride (NbN) wire. (b) When a photon is absorbed in the wire, the energy of the photon is typically enough to break thousands of Cooper pairs. This destroys the superconductivity, forming a resistive region in a small volume of the wire called the hotspot[15, 16]. Supercurrent is then forced to flow around the hotspot causing the current density in these regions to exceed $j_c$. (c) Subsequently a resistive barrier forms across the wire is giving rise to a measurable voltage pulse at the terminals of the wire. (d) Finally the energy dissipates in the form of substrate phonons and the system returns to its initial state.

The size of the hotspot is determined by a balance between the quasiparticle diffusion rate and recombination rate. For 1550 nm wavelength photons in a thin film of NbN, the hotspot size is approximately tens of nanometers in diameter as shown in simulation results based on the hotspot model presented in section 4.4.1.

## 1.4 Description of the SN-SPD

The SN-SPD consists of a 4-nm-thick, $\sim$ 100-nm-wide superconducting NbN wire operating at 4.2 K or below. The $T_c$ of the NbN film is about 10.5 K and the $j_c$ of the film is 2 to 6 MA/cm$^2$ [9]. Figure 1-2 shows an example of an SN-SPD that we fabricated. The nanowire is typically folded and spaced closely in a meander (boustrophedonic) structure in order to increase the "active area" of the detector which is the area occupied by the nanowire (center of figure 1-2 (left)).

## 1.5 Requirements for nanowire dimensions and smoothness

To detect photons efficiently, nanowires need to be narrow ($\leq$ 100 nm), free of severe constrictions and linewidth non-uniformity. As shown in figure 1-3, a severe constriction can be thought to be anything larger than the dimension of the hotspot ($>$ 10 nm). In figure 1-3, the absorbed photon will not be detected as the increased current

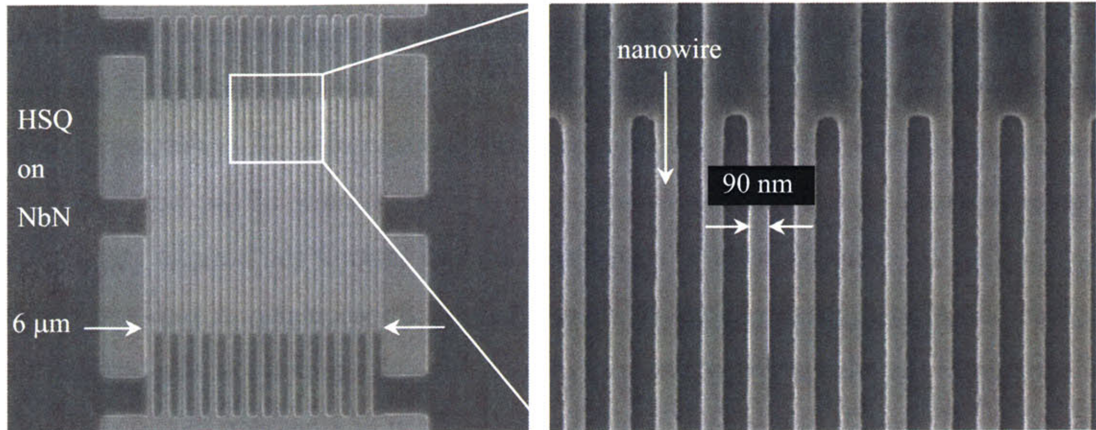


Figure 1-2: (Left) Scanning electron micrograph (SEM) image of a patterned electron beam resist on NbN film. (Right) SEM image of a zoomed in view of the meander. The active area consists of 90 nm wide nanowires folded tightly in a meander structure.

density around the hotspot is still less than the critical current density, $j_c$.

Severe constrictions will reduce the $I_c$ of the nanowire because current densities are highest at the narrowest parts of the wire. Consequently, the constrictions are the only points in the detector that can detect photons. The other wider parts of the wire are less sensitive because the current densities here are much less than $j_c$. In other words, the supercurrent can still flow around hotspots formed in the wider portions without exceeding $j_c$. SN-SPDs with non-uniform linewidth nanowires and constrictions will have low DEs.

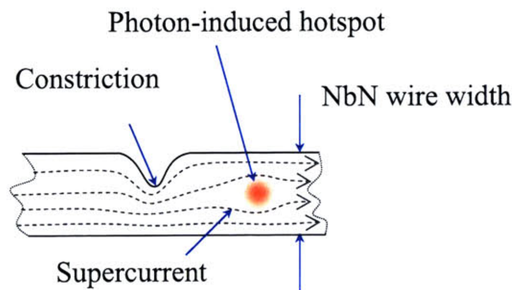


Figure 1-3: A schematic drawing of a nanowire with a severe constriction where the current density is highest.

The DE of SN-SPD is currently too low for most applications (ref. section 1.1). Several factors that may be limiting DE and ways to overcome them are as follows:

1. Only a small fraction of incident photons are actually absorbed by the detector while the rest are either transmitted through or reflected off the detector. We can increase the absorption and therefore the DE by (1) using thicker and more optically absorptive NbN films, (2) increasing the fill factor of the detector (i.e. reducing the spacing between nanowire), (3) increasing the length of the nanowire (and thus the total area of the meander) and (4) fabricating an anti-reflection coating and an optical resonator (to enhance the electric-field intensity at the detector).

2. Even if every incident photon is absorbed, an absorbed photon may have still have a low chance of being detected because the nanowire width is much larger than the hotspot size. We can overcome this limitation by making narrower nanowires ($\leq$ dimension of the hotspot); so that an absorbed photon generates a hotspot that immediately forms a resistive barrier across the nanowire.

3. As explained previously, the DE may be limited due to wire nonuniformity and/or narrow constrictions along the wire. To increase the DE of the detector, we should ensure uniform nanowire linewidth along the entire wire.

4. The NbN film quality may have been degraded due damage during fabrication or during sample handling. Identifying and minimizing sources of material damage (such as electro-static-discharge damage, plasma damage, thermal damage, and chemical damage) will help improve DE.

5. Our current high-speed test equipment does not have sufficient signal-to-noise ratio to test nanowires narrower than $\sim$ 75 nm. Narrower wires have lower $I_c$s and therefore lower output signals. One possible solution is to amplify the signal from narrower wires using an on-chip readout circuitry. This circuit will enable us to test SN-SPDs with linewidths at the dimension of the hotspot.

## 1.6 Objectives and challenges

The main objective of this project was to develop a fabrication process to make working SN-SPDs at MIT. This fabrication process was designed to be as simple as possible while providing better nanowire linewidth uniformity control compared to the process used in [8]. Sapphire wafers with epitaxially grown thin-film (4 nm) superconducting NbN were purchased from G. Gol'tsman's group in Moscow to be used as the starting material.

Although improving the DE of the detector was not the main concern in this project, steps in the right direction were taken to fabricate working SN-SPDs that should have improved DEs. The fabrication challenges were:

1. to make highly uniform nanowires,
2. to make nanowires packed tightly together with narrow gaps (i.e. high fill factor)
3. to make large area meanders
4. to do all the above without impairing the superconductivity of the NbN films.

The next step after developing a working process was to test the superconductivity of the SN-SPDs. This test ensured that the process did not damage the material. The final objective was to test the SN-SPD's single-photon detection capabilities in high-speed electrical measurements.

## 1.7 Summary of work done in this project

We developed a new fabrication process for making SN-SPDs [17]. Figure 1-4 illustrates the process flow for fabricating SN-SPDs with require only a single alignment step. In this new process, the negative tone electron resist, hydrogen silsesquioxane (HSQ) was used. Using a negative resist simplifies the process by reducing the number of fabrication steps. HSQ was the resist of choice due of its high resolution [18], low line-edge roughness [19] and negligible absorbance down to 157-nm wavelengths

[20]. Low absorption at 1550 nm will allow us to integrate HSQ into a later part of the project as a dielectric layer in building an integrated optical cavity for enhancing DE.

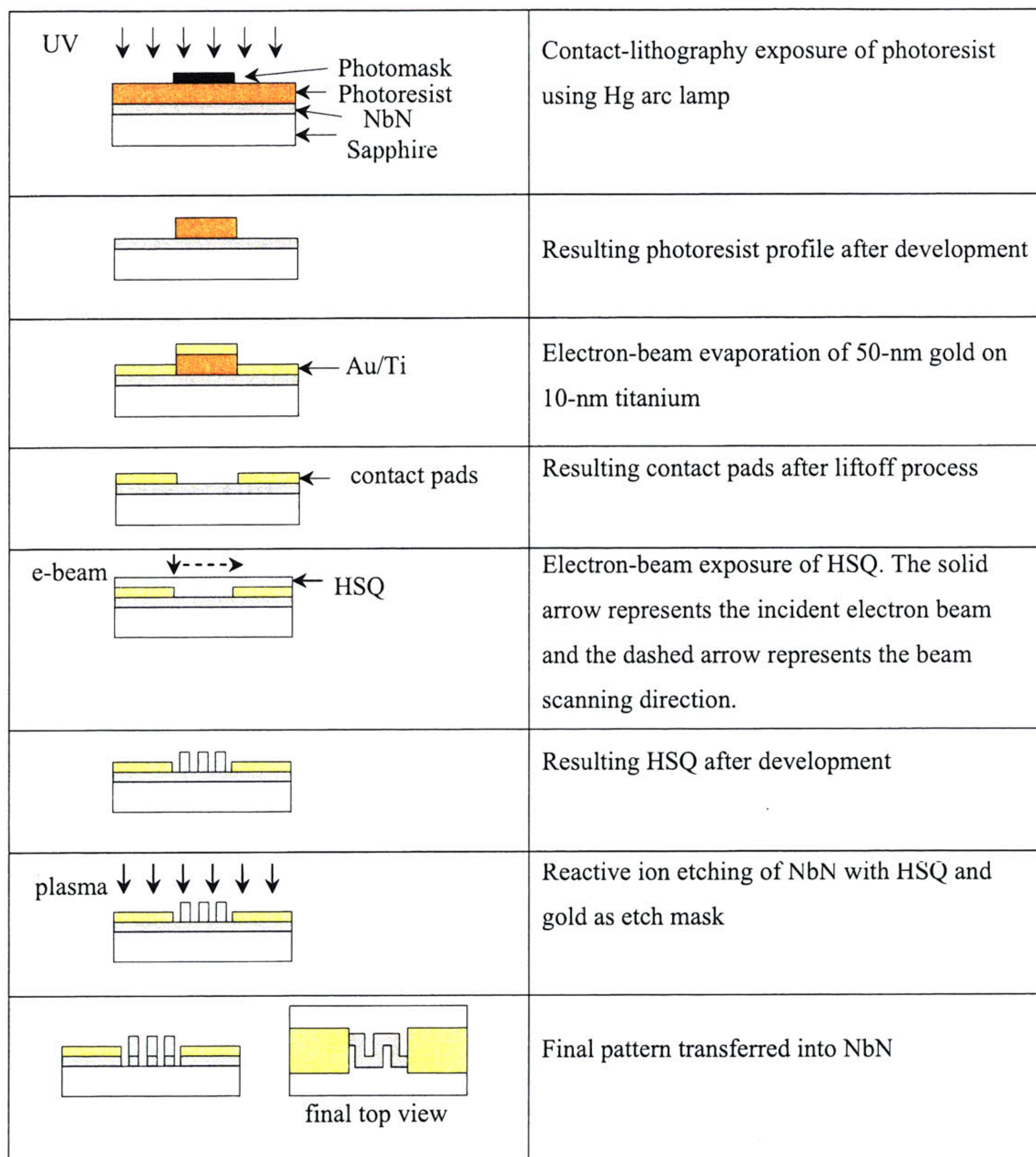


Figure 1-4: Process flow for fabricating SN-SPD.

It was difficult to develop a process that did not damage the superconductivity of the film. Section contains more details on material damage due to fabrication process and sample handling.

Here is a summary of work done in fabricating and testing SN-SPDs.

1. Contact photolithography and liftoff process were developed to create gold contact pads. In Chapter 2 we explain the details of the process and the challenges of getting good liftoff especially with small samples. We found that the key to a successful liftoff was to have an undercut structure in the photoresist sidewalls.

2. Nanowire structures were fabricated using electron-beam lithography (EBL) and reactive ion etching (RIE) as explained in Chapter 3. A proximity effect correction (PEC) program was written to design meander patterns that will yield SN-SPDs with excellent linewidth uniformity using HSQ as the electron resist.

3. Nanowires of varying widths were tested at cryogenic temperatures. Chapter 4 explains device functionality and performance tests. High speed tests were done that verified photosensitivity of the detectors.

# Chapter 2

# Defining gold contact pads

Gold contact pads provide electrical connection between the SN-SPDs and the external world. Connection can be made to the contact pads either through the probe pins of a cryogenic probing station or by wirebonding the contact pads to a chip holder.

For high-speed electrical measurements, the contact pads also act as coplanar-waveguide (CPW) transmission lines. Figure 2-1 shows how the CPW connects to the SN-SPD. As shown, the CPW consists of a central metal strip which carries the signal and a surrounding ground plane. The ratio of the central strip width, $W$, to the gap, $s$, is constant as the CPW tapers down to match the smaller dimensions of the SN-SPD. By adjusting $W : s$ ratio, the contact pads can be designed to the desired impedance value. The contact pads that we use were designed to have $\sim 50$ $\Omega$ impedance with $W = 100$ $\mu$m and $s = 65$ $\mu$m.

In addition to contact pads designed as CPW transmission line for high speed measurements, some were also designed for four-point-probe DC tests to measure the sheet resistance of the NbN film. The designs were sent to Advanced Reproductions Corporation to be made into a chrome-on-glass, 4-inch photomask. The smallest feature on the mask was 6 $\mu$m.

The starting material, a 3-cm by 3-cm square sapphire chip with an epitaxial 4-nm-thick NbN film, was sent to Valley Design Corporation to be diced into 3.5-mm-by-3.5-mm samples. Dicing the wafer into many smaller pieces allowed us to do different experiments on each sample without using up an entire wafer. Defining gold

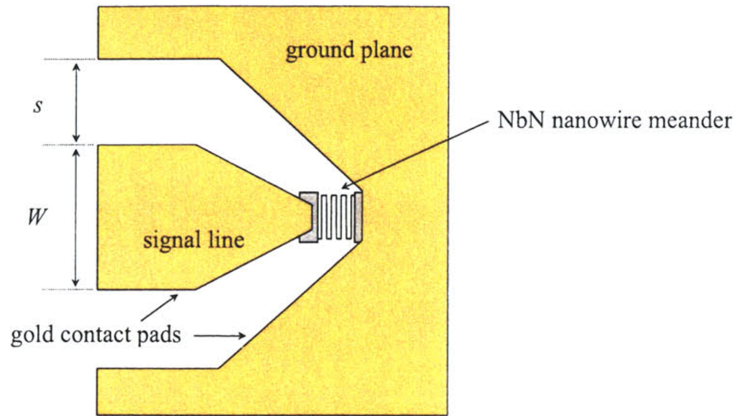


Figure 2-1: Diagram of a coplanar waveguide (CPW) connected to the SN-SPD.

contact pads on the small samples is the first processing step in making SN-SPDs.

## 2.1 Liftoff process

Liftoff is an additive pattern-transfer technique that is commonly used for patterning metal on substrates. It involves the addition of metal films through a resist mask onto a substrate. Generally, the liftoff process includes steps as shown in figure 2-2.

First, the desired pattern is exposed in photoresist using UV light through a photomask. Next, the sample is immersed in a photoresist developer. For positive tone photoresists, UV exposed regions dissolve in and are removed by the developer. The opposite is true for negative tone photoresists. In figure 2-2, a positive tone photoresist is used. After development, the result is a photoresist layer with openings through which metal will be deposited onto the NbN film. In other words, the resist masks sample areas where metal is not wanted.

Electron-beam evaporation deposits the desired metal film uniformly over the entire sample. In an electron-beam evaporator chamber, a high energy electron beam heats up and evaporates a small spot on a metal target. Evaporated metal atoms then move towards the sample, placed a distance away from the target. Due to low pressures in the chamber, metal coats the sample surface directionally. Only surfaces in the line of sight from the target will be coated. Therefore, to achieve a good

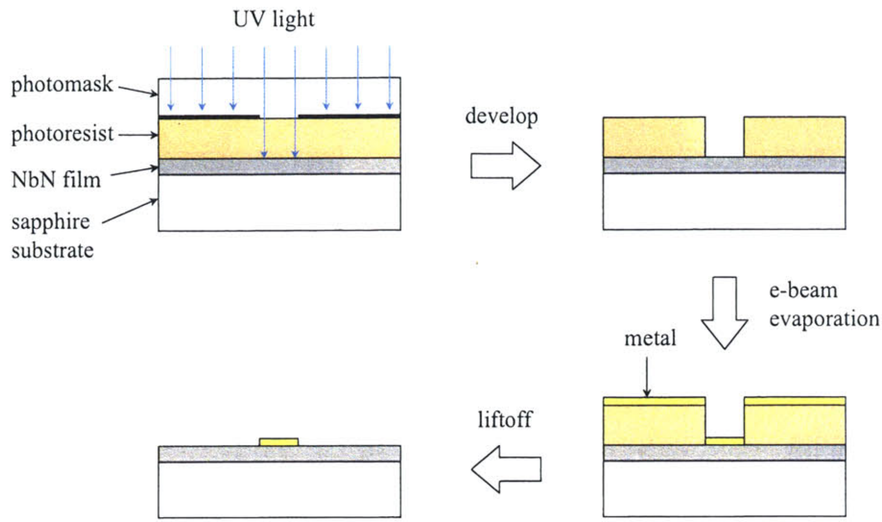


Figure 2-2: Process flow for liftoff.

liftoff, we need to create a discontinuity between metal on the NbN surface and on the resist. This can be done by establishing a vertical or an undercut profile in the resist sidewall.

In the final step, resist is dissolved away in an organic solvent and unwanted metal (on the resist) separates from the sample surface leaving only the desired patterned metal on the sample.

## 2.2 Challenges in liftoff for small samples

Unfortunately, the resist sidewall profile is often not vertical but sloped. In this case, as shown schematically in figure 2-3, metal will also coat the sidewalls, forming a continuous film over the entire surface. Consequently, the final liftoff step becomes problematic. Metal film will tear unpredictably or could peel off the NbN surface.

Liftoff is particularly problematic for small samples (3.5 mm by 3.5 mm and less) due to edge beads. Edge beads refer to the thick residual resist that forms at sample edges during spin coating. Edge beads cause sloped resist sidewalls (ref. section 2.3.1). During spin coating, the centrifugal force on the edge resist on a small sample is lower than for a larger sample. This causes edge beads to form more readily on

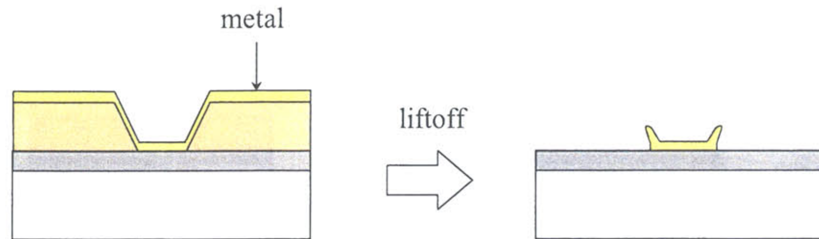


Figure 2-3: Sloped sidewalls cause problematic liftoff.

smaller samples.

## 2.3 Contact printing photolithography

In contact photolithography, resist-coated sample is in physical contact with a glass photomask. Photoresist is exposed by collimated UV light from a Mercury arc lamp while the wafer is in contact with the mask.

### 2.3.1 Ideal contact printing photolithography and effect of edge beads

Figure 2-4 (a) illustrates an ideal situation when perfect contact between mask and resist is achieved. Due to the intimate contact between mask and resist, the light intensity profile in the resist is very well confined to the shape of the mask opening as shown at the bottom of 2-4 (a).

When spin coating small sapphire samples, edge beads form at the corners. Edge beads cause a gap to form between photomask and photoresist during contact photolithography, as illustrated in figure 2-4 (b). Due to diffraction, the light intensity profile in the resist will be broadened and have a more gradual slope as compared to the previous case of perfect contact.

The broadened intensity profile in the resist results in sloped resist sidewalls. This effect can be understood by studying figure 2-5. Figure 2-5 shows the dependence

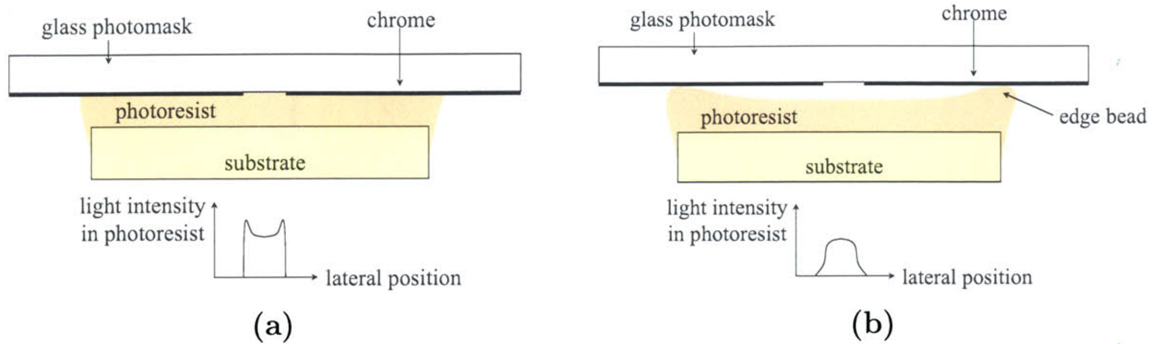


Figure 2-4: a) Ideal contact photolithography setup. b)Case when edge beads are present.

of the resultant resist profile (quadrant 4) on exposure intensity (quadrant 1), resist contrast (quadrant 2) and development time (quadrant 3).

Quadrant 1 shows the exposure intensity profile in the resist when the mask is not in intimate contact with the resist. Quadrant 2 is the resist contrast curve showing that highly exposed regions have a higher resist removal rate during development. Quadrant 3 relates the development rate to the actual amount of resist removal. The slope of the line in quadrant 3 is dependent on the development time. The plot in quadrant 4 is obtained by joining the points from the plots of quadrants 1 to 3 and shows the final resist profile. The dashed lines are just examples of how a few points are connected. The result in quadrant 4 shows that the resist profile has sloped sidewalls.

We can imagine that (1) increasing the exposure dose by increasing the exposure time and (2) increasing the development time will both make the sidewall profile more vertical. However, doing so will increase the dimensions of exposed regions leading to poor critical-dimension control. Other effects such as light absorption in the resist will also contribute to cause the sloped resist profile.

## 2.4 Process details

We developed a working process for creating overhang structures in the resist sidewalls to overcome the problem caused by edge beads, therefore permitting good liftoff. In

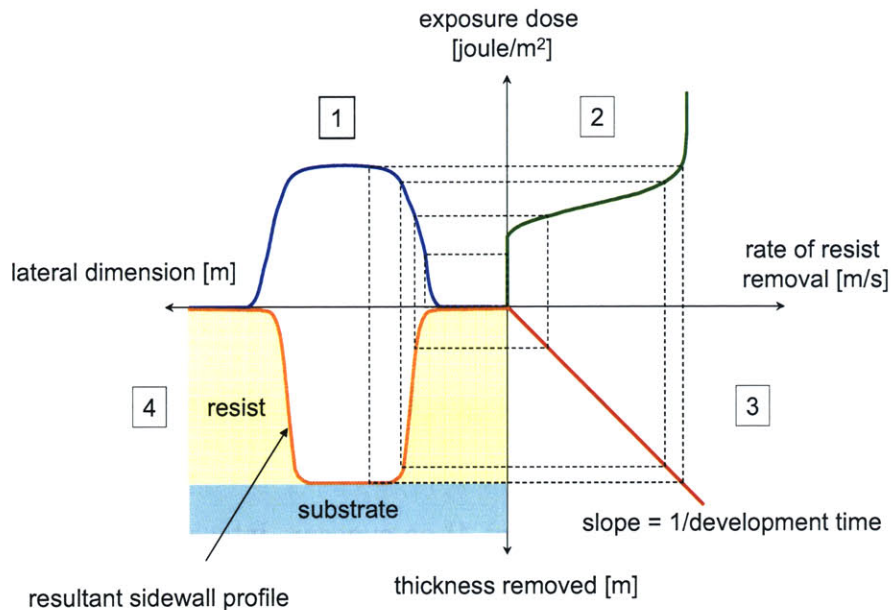


Figure 2-5: Relationship among exposure dose, resist contrast, development time and resultant resist profile.

the following sections, the details of the process is presented. This process works equally well for both small and large samples.

### 2.4.1 Resist spin coating

The samples were first rinsed in acetone followed by deionized (DI) water and blown dry using $N_2$. Next, a drop of Shipley Microposit S1813 positive photoresist is spin coated onto the sample at 6 krpm. Spin coating at a high speed helps to reduce the formation of large edge beads but does not eliminate them completely.

Edge beads form readily due to the moderately high viscosity of the S1813 photoresist. Spining at 6 krpm results in a photoresist thickness of about 1 $\mu$m.

During spin coating, the solvents in the photoresist evaporate and the resist flattens out. The final resist thickness, $d$, depends on resist concentration, $k$, and spin speed, $\omega$. Equation (2.1) was found to be true for several different types of resist. The spin curve (thickness vs. spin speed) for S1813 is shown in figure 2-6 where the dotted line is a best fit to measured data. The fitting equation agrees well with equation (2.1).

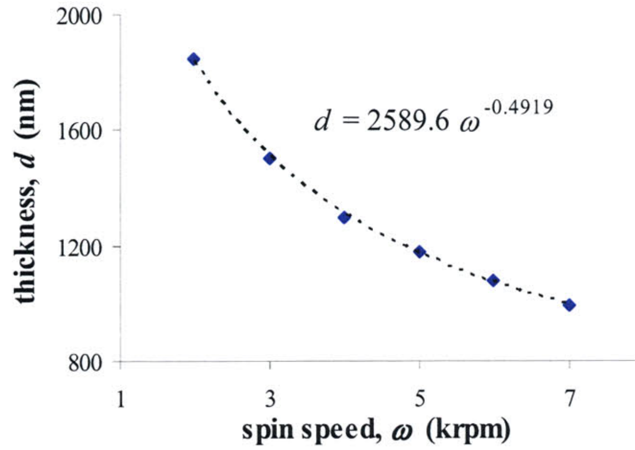


Figure 2-6: Spin curve for Shipley Microposit S1813.

$$d \propto \omega^{-0.5} \tag{2.1}$$

After spin coating, the samples were soft-baked at 90 °C for 2 minutes to drive out excess solvents. Although the S1813 data sheet recommends soft-baking at 115 °C for 1 minute, baking at a lower temperature reduced the possibility of damaging the NbN film.

### 2.4.2 Contact photolithography

Contact photolithography was performed using the Tamarack mercury arc lamp UV source in the Nanostructures Lab. The source has both 365 nm (mercury i-line) and 220 nm (mercury g-line) wavelengths in its spectrum. The photomask was aligned to one sample at a time by eye. Exposure was done for 25 s at 4500 $\mu$W/cm$^2$ intensity. As explained in section 2.3.1, a shorter exposure time causes more highly sloped sidewalls while a longer exposure causes more vertical sidewalls but poor critical dimension control. The 25 s exposure was found to be a good compromise, resulting in feature sizes that are $< 1$ $\mu$m larger than intended.

### 2.4.3 Creating an overhang structure

We created an overhang structure in the resist using a process adapted from that proposed by Hatzakis et. al. [21]. To create the overhang structure, the samples were soaked in chlorobenzene for 10 minutes at room temperature prior to development. Samples taken out of chlorobenzene have to be blown dry using a $N_2$ gun before immersing in the developer. This removed chlorobenzene from the sample surface. Any residual chlorobenzene may act as a barrier between the developer and the photoresist.

During the chlorobenzene soak, chlorobenzene removes residual solvent and low-molecular-weight resin from the resist surface, thereby reducing the solubility of the resultant modified resist layer in the developer. The result of chlorobenzene soak is shown in figure 2-7.

In figure 2-7 (a) the sample was soaked for only 5 minutes. This was sufficient to create an overhang/undercut of approximately 400 nm. In figure 2-7 (b) we increasing the immersion time to 10 minutes resulting in a thicker and longer overhang. Due to the removal of substances from the resist, tensile stress is generated in the surface which results in a slight detachment of the photoresist from the substrate and an upward curl in the resist edge.

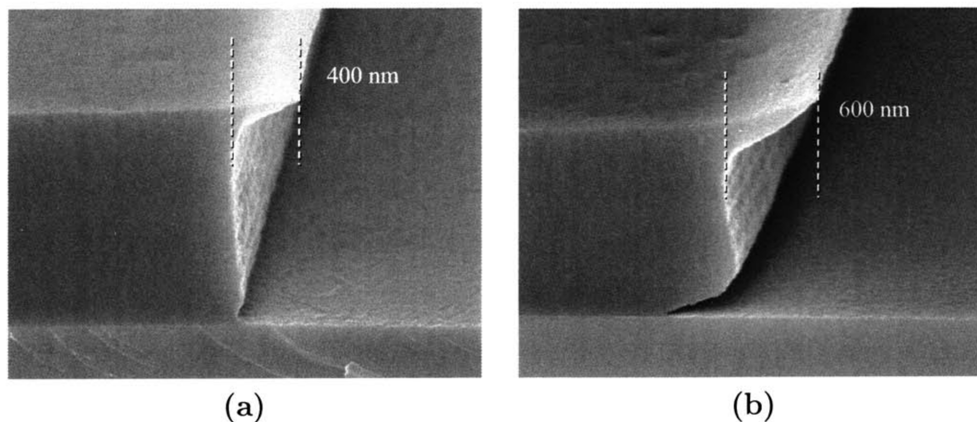


Figure 2-7: SEM image of overhang structures in S1813 photoresist on silicon created by immersion in chlorobenzene prior to developemnt.

### 2.4.4 Photoresist development

A NaOH-based developer, Shipley Microposit MF 352, is used to remove exposed photoresist. Development is done by immersing the samples into the aqueous solution for 3 minutes, gently agitating the developer periodically to maintain fresh solvent supply across the sample. After the first few seconds, development is observable when the exposed resist dissolves in the developer to form a dark red solution that diffuses away from the sample surface. Finally, the samples are taken out from the developer and rinsed in DI water for about 30 s, then blown dry using a $N_2$ gun.

### 2.4.5 Metal deposition by electron-beam evaporation

Metal is deposited onto the sample via electron-beam evaporation. A 10-nm layer of titanium (Ti) is deposited onto the sample before depositing a 50-nm thick layer of gold (Au). Although we did not try depositing Au directly onto NbN, we believe the Ti layer improves adhesion between Au and NbN as it has been traditionally used as an adhesion layer between metal and substrate. Metal thickness was kept to a minimum to aid the planarization of electron-beam resist during spin coating in a later step.

### 2.4.6 Heating effects of metal deposition

We were concerned that electron-beam evaporation causes thermal damage to NbN. This lead us to calculate for the temperature increase at the NbN surface due to metal deposition. We found that even though the evaporated metal atoms reaching the sample are extremely hot, the total amount of heat transferred to the sample does not increase its surface temperature significantly.

We calculated the increase in temperature at the sample surface due to a constant rate of titanium deposition on a 1 mm thick sapphire substrate. The calculation is based on the simple heat equation (2.2) below.

$$Q = \sigma \frac{dT}{dx} = \rho_{Ti} R [C_v (T_{boil} - 300 \text{ K}) + C_{evap} + C_{fusion}] \tag{2.2}$$

where,

$$
\begin{aligned}
Q &= \text{heat flow per unit area} && (2.3)\\
\sigma &= \text{thermal conductivity of sapphire} = 40\ \text{W/m/K} && (2.4)\\
\rho_{Ti} &= \text{density of titanium} = 4.5\ \text{g/cm}^3 && (2.5)\\
R &= \text{titanium deposition rate} = 0.5\ \text{nm/s} && (2.6)\\
C_v &= \text{specific heat capacity of titanium} = 523\ \text{J/K/kg} && (2.7)\\
C_{evap} &= \text{latent heat of evaporation of titanium} = 8893\ \text{J/g} && (2.8)\\
C_{fusion} &= \text{latent heat of fusion of titanium} = 365\text{J/g} && (2.9)\\
T_{boil} &= \text{boiling point of titanium} = 3287\ {}^\circ\text{C} && (2.10)\\
& && (2.11)
\end{aligned}
$$

Assume that the sample stage temperature is kept at 300 K and the sample is in good thermal contact with it, then:

$$
\begin{aligned}
\frac{dT}{dx} &= (T_{surface} - 300\text{K})/(\text{substrate thickness}) && (2.12)\\
\text{substrate thickness} &= 1\ \text{mm} && (2.13)\\
T_{surface} &= 300.0006\ \text{K} && (2.14)
\end{aligned}
$$

The calculation shows that the increase in substrate surface temperature due to the deposition of titanium is negligibly small. It is likely that thermal radiation from the metal target is the dominant heating effect during electron-beam evaporation. Even so, we have observed no severe heating effects. As shown in figure 2-8, the entire metal deposition process does not melt or deform the resist. Hence we conclude that sample temperature does not increase beyond resist melting or deformation temperature ($\sim$ 100 °C).

Notice the discontinuity between the metal on the resist and the substrate, a result

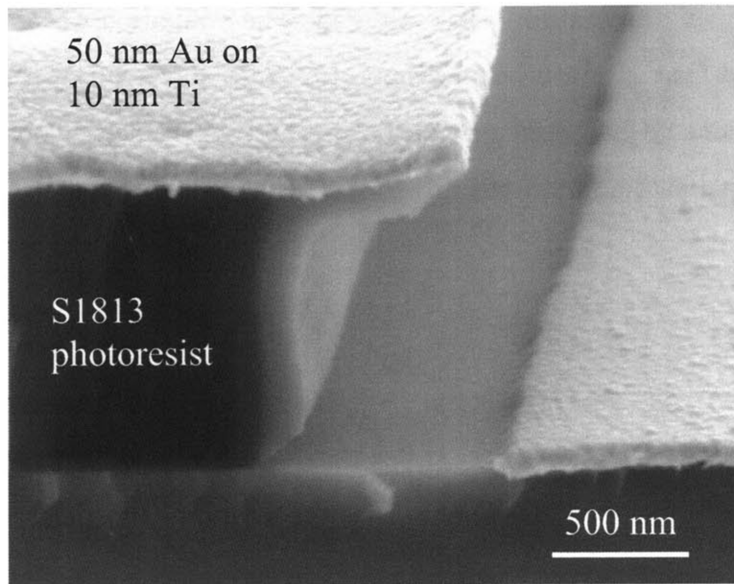


Figure 2-8: SEM image of an overhang structure after 10 nm of Ti and 50 nm of Au have been deposited by electron-beam evaporation.

of the directional nature of metal deposition. This discontinuity ensures good liftoff in the final step.

### 2.4.7 Final liftoff step

In the final step of patterning the gold contact pads, the unwanted metal on top of the photoresist was removed by dissolving the photoresist in the solvent, n-methyl-pyrrolidone (NMP) at 90 °C until liftoff is complete. With resist overhang structures, the process usually took less than a minute.

Finally, the samples were removed from hot NMP, rinsed in acetone to cool it down before rinsing in DI water and blown dry.

## 2.5 Summary

In this chapter, a method of defining gold contact pads using liftoff was presented. We explained that edgebeads caused sloped resist sidewalls on small samples and resulted in poor liftoff. Then, we presented a technique for creating overhang structures in the resist sidewalls to achieve good liftoff. Finally sample heating during metal deposition

(via electron-beam evaporation) was evaluated. The evaluation was done because we were concerned that electron-beam evaporation may have caused thermal damage to NbN. We concluded (based on calculation and experimental observation) that negligible sample heating occurred.

# Chapter 3

# Patterning nanowires in NbN

With the contact pads in place, nanowires are then fabricated to bridge a 15-$\mu$m gap between the signal and ground pad. Nanowire patterns were exposed in a negative-tone electron resist, hydrogen silsesquioxane (HSQ), using electron-beam lithography (EBL) followed by a final pattern transfer into NbN by reactive ion etching. Alignment marks that were also defined during the liftoff process allow the nanowire patterns to be aligned to the gold contact pads during during EBL exposure. This is the only alignment step needed in the entire SN-SPD fabrication process.

A proximity-effect-correction program was developed to helps us achieve uniform linewidths in the SN-SPD meanders. This program, based on a double-gaussian model of the electron-beam, pre-compensates the pattern design by taking into account electron-beam broadening effects that occur during resist exposure.

## 3.1 Electron-beam lithography

Electron-beam lithography (EBL) is a lithographic process where a tightly focused beam of highly accelerated (10-50kV) electrons is used to define high resolution patterns in electron-beam resist. A Raith 150 electron-beam lithography system was used in this project. It has a thermal-field emission source, a Gemini electron-optics column and offers the flexibility of variable acceleration voltages from 200 V to 30 kV. The minimum linewidth achievable with this system is $\sim$ 17 nm at 30 kV [22].

Unlike contact printing photolithography, EBL does not need a physical mask to transfer patterns into the resist. Instead, in the Raith 150, the intended pattern is designed using a GDSII format layout-editor software. The EBL system then simply 'writes' the designed pattern in electron resist using the electron beam as its pen. This serial manner in which patterns are exposed makes EBL exposures slow. Therefore, EBL is more suitable for defining high resolution (sub-micron) features as compared to exposing large areas (> 100 $\mu$m).

## 3.2 Proximity effects in EBL

As the electrons penetrate the resist, they scatter, due to collisions with atoms in the material, and change trajectory. Figure 3-1 illustrates the trajectory of a few electrons as they penetrate a resist coated substrate.

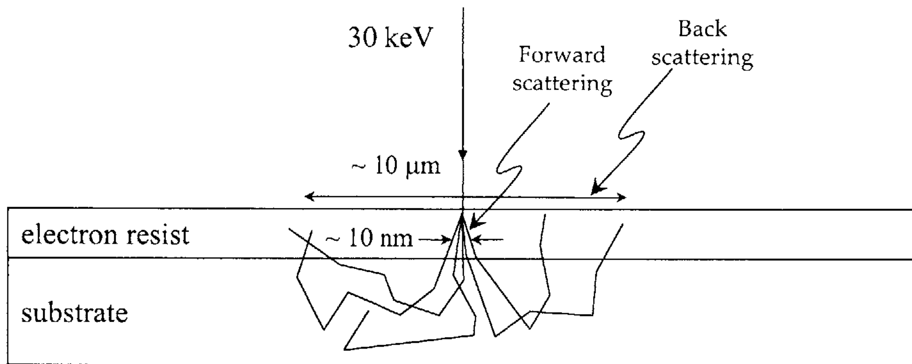


Figure 3-1: An illustration of forward and backward scattering of the electron beam during exposure.

The initial broadening of the incident beam due to scattering in the resist is known as forward scattering. Forward scattering determines the EBL resolution (typically 10 nm in diameter). As the electrons penetrate the resist, they 'expose' the resist either by chemical bond scission or formation. The electrons then penetrate into the substrate after passing through the resist. The scattering events in the substrate causes some electrons deflect out of the substrate and back into the resist. This backward deflection, called backscattering, causes additional resist exposure. The

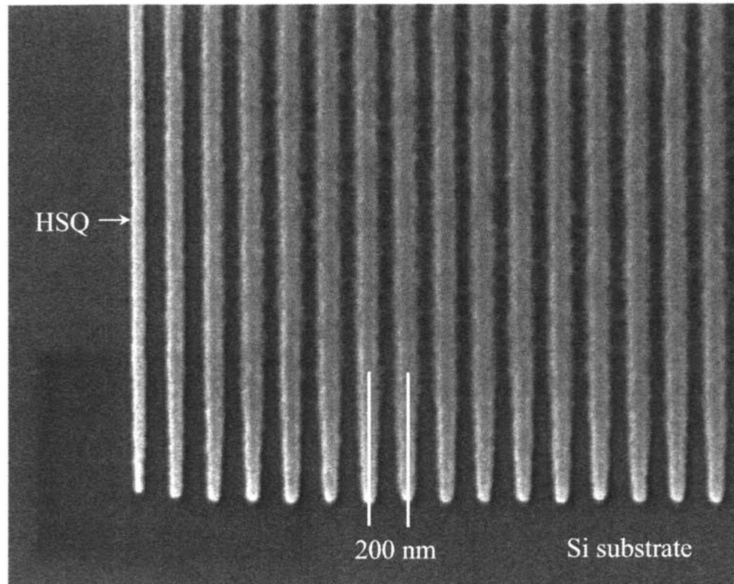


Figure 3-2: SEM image showing one corner of a 200 nm period grating written in HSQ at 10 kV using the Raith 150 EBL.

backscattering range can be large (about 5 to 10 $\mu$m depending on the beam acceleration voltage).

Backscattering causes unintended resist exposure in the regions around the intended patterns. The combination of forward and backward scattering is known as proximity effects in EBL. Figure 3-2 shows an example of a proximity-effected grating pattern. The grating was written in hydrogen-silsesquioxane (HSQ), a negative-tone electron resist. In this example, proximity effect is the unintentional exposure in between the grating lines causing footing/scumming/bridging between the dense lines. The effect is worse where the lines are dense (top right of image). The linewidths also decrease as the pattern density decreases towards the left and bottom edges of the grating where the pattern is less dense. Therefore proximity effects cause footing in between dense lines and non-uniform linewidths in the grating.

In the fabrication of the detectors, it is important that the nanowires have uniform widths (ref section 1.5). To achieve this, we need to compensate for proximity effects. This compensation, called proximity effect correction, is done by modeling the electron beam followed by designing the meander pattern such that the calculated doses on the lines are uniform.

## 3.3 Modeling the electron beam

The forward and backward scattering of the electron can be modeled using a double-gaussian approximation for the exposure dose [23]. Exposure dose is a measure of the degree of exposure in the resist. In EBL, It is defined as charge per unit area [$\mu$C/cm$^2$].

The resultant point exposure dose distribution in the electron resist can be expressed as the point spread function (PSF) as in equation (3.1).

$$PSF(r) = \frac{1}{\pi(1+\eta)}(\frac{1}{\alpha^2}e^{-(\frac{r}{\alpha})^2} + \frac{\eta}{\beta^2}e^{-(\frac{r}{\beta})^2}) \tag{3.1}$$

The variables are defined as follows:

- $r$ - radial distance from the point of incidence,
- $\alpha$ - characteristic half width of the dose distribution due to forward scattering,
- $\beta$ - characteristic half width of the dose distribution due to backscattering,
- $\eta$ - ratio of backward to forward scattered electron distribution.

For exposures at 30 kV, with sapphire as the substrate, we used the following parameter values as suggested in the Raith 150 software:

1. $\alpha = 0.01$ $\mu$m;
2. $\beta = 2.436$ $\mu$m;
3. $\eta = 0.5$.

A few methods could actually be used to experimentally determine the point-spread-function parameters [24, 25, 23]. We did not determine the parameters in a separate experiment as the suggested parameters were sufficiently accurate for the intended purpose.

The first and second terms in equation 3.1 model the forward and backscattered electron dose distribution respectively. A higher acceleration voltage results in a

smaller forward scattering range (a smaller $\alpha$ value) but a larger backward scattering range (a larger $\beta$ value). This happens because the electrons are deflected less upon entering the resist but have more energy to scatter over larger distances. $\eta$ is a substrate-dependent parameter and increases with the average atomic number of the elements in the substrate. For example, $\eta$ for sapphire ($Al_2O_3$) with average atomic number of 10 is 0.5 and $\eta$ for silicon with an atomic number of 14 is 0.7.

From the perspective of system engineering, PSF is the delta-function response of the EBL system. In other words, when the "input function" into the EBL is a delta function, the "output function" will be the PSF. This fact immediately allows one to calculate the maximum spatial frequency, $k_r$, of the designed pattern that can "pass through" the EBL system. By looking at the fourier transform of the PSF in equation (3.2) we see that resolution $< 2\alpha$ is impossible.

$$\boldsymbol{F}(PSF(r)) = \frac{1}{\sqrt{\pi}(1+\eta)}(\frac{1}{\alpha}e^{-(\pi k_r \alpha)^2} + \frac{\eta}{\beta}e^{-(\pi k_r \beta)^2}) \tag{3.2}$$

## 3.4 Proximity-effect correction

We developed a simple program in Matlab to calculate proximity effects in the Raith EBL using the double-gaussian model for the electron beam. The program first generates an "input" matrix. This matrix is a the layout map of the meander pattern and has non-zero elements only where exposure is intended. Then it does a 2D convolution between the input pattern with the PSF to get the resultant "output" dose distribution.

Convolution was done by calculating the fourier transforms of the input and the PSF, calculating their product in frequency domain and converting the product back into the spatial domain.

PEC can be done either by dose modification or pattern shape modification [26, 27]. A combination of the two was used to achieve uniform dose distribution on the lines in the meander active area, resulting in good linewidth uniformity.

In the fabrication of SN-SPDs, it is the linewidth uniformity in the detector active

area that matters. The critical dimension control of the features surrounding the active area is less important. These features only provide a bridge between the SNSPD and the gold contact pads. The sizes and doses of the surrounding features can therefore be used to flatten out the dose distribution at the active area. Additional dummy features at the edges of the meander can also be introduced to help achieve this.

The Raith software accepts layouts in the GDSII format and has a GDSII file editor. In the GDSII editor, patterns are defined using either dots, lines or polygon elements. The meander was designed using only rectangular elements as shown in figure 3-3.

Raith 150 will expose the area within a rectangle using a single areal dose setting. Hence dose adjustments are made by assigning the appropriate doses to the rectangles around the active area such that the resultant dose distribution at the active area is uniform.

The objective of the PEC was to achieve a uniform dose distribution at the meander lines. To do this, several iterations of the following steps were done manually.

1. First, the 2D convolution was done to get the proximity effected meander pattern.

2. Then, doses at points on the meander lines across the entire meander area were sampled. The Matlab *surf* function was used to plot this data in 3D. This plot gave an indication to the adjustments that were needed to achieve a more uniform dose distribution at the meander lines.

3. Adjustments were then made to the input pattern by:

    (a) adjusting the dose of the features around the meander lines,

    (b) adjusting the distance between the features and the meander,

    (c) adjusting the sizes of the surrounding features,

    (d) adding dummy features at the top and bottom of the meander.

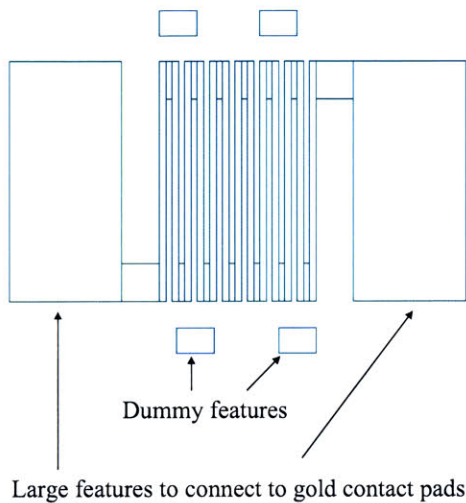


Figure 3-3: Layout of the meander design as it appears in a GDS2 file editor.

4. The process was repeated

PEC was complete when the maximum dose variation on the lines across the meander active area was less than 0.1 % of the average dose received at the lines. Small variations in the dose could be observed visually by plotting the output dose distribution using a different colormap (see figure 3-4). Once PEC was complete, the Matlab program generated the corrected input pattern in an ASCII (*.asc) file format that the Raith software could understand.

Figure 3-4 shows the simulated resultant dose distributions without PEC (a) and (c) and after PEC (b) and (d). Notice the addition of dummy features at the top and bottom of the active area in (b) and (d). Figure 3-4 (c) and (d) are the same as (a) and (b) respectively but are plotted using a different colormap to accentuate slight dose differences. Notice in figure 3-4 (c) that the left and right edges of the active area receive a higher dose than at the center. This dose variation will cause lines at the edges to be wider than at the middle. After PEC, the meander active area has uniform dose distribution as can be seen in figure 3-4 (d) where the lines are at the same color (purple).

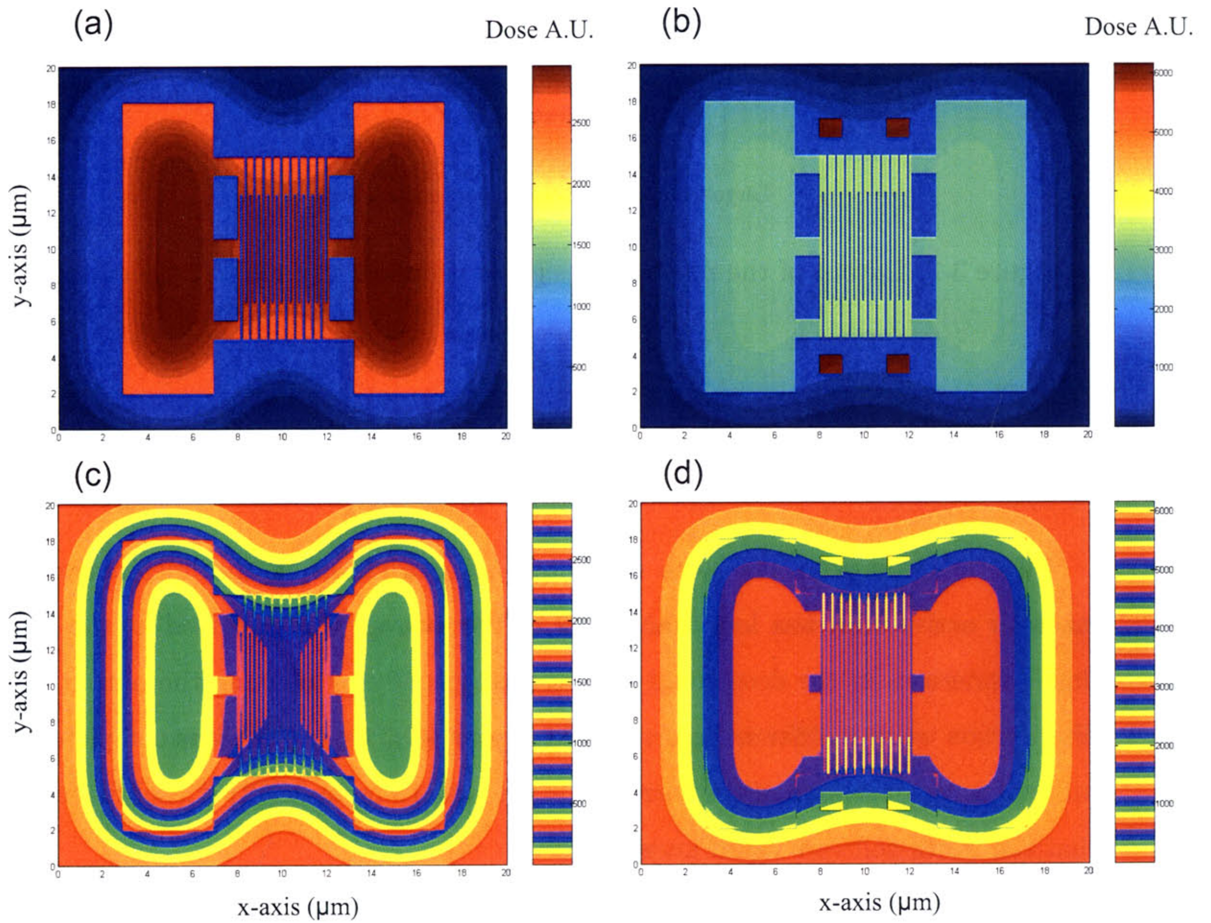


Figure 3-4: Matlab simulation plots of areal dose (shown using different colors) at every position of the meander pattern.

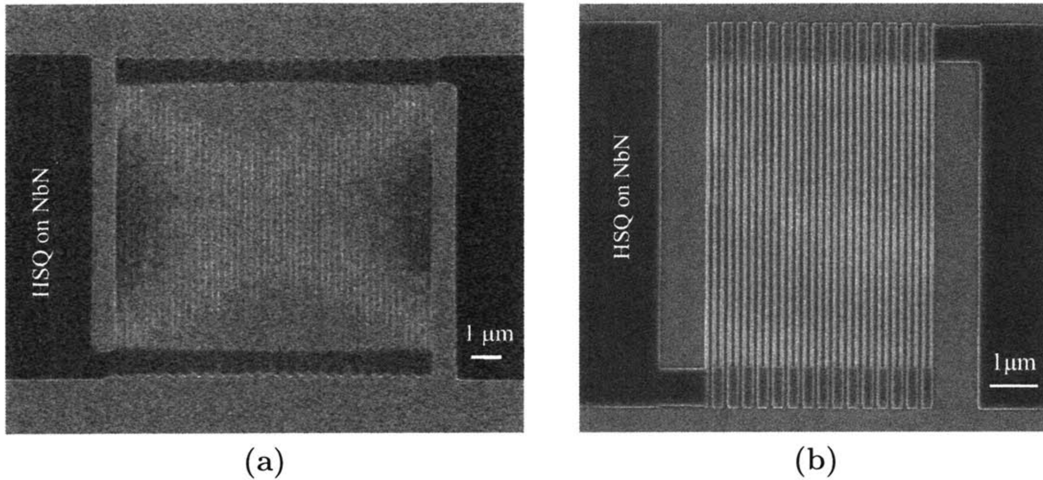


(a) (b)

Figure 3-5: SEM image of meander patterns written in HSQ before (a) and after (b) the PEC program was developed and used.

## 3.5 Experimental results

The PEC program generates the corrected "input" pattern that will produce the best possible results when written in the Raith EBL. It allows one to predict experimental results without having to do time-consuming experimental iterations.

The following are several experimental results that demonstrate the accuracy and usefulness of the PEC program.

### 3.5.1 Quantitative measurement of linewidth variation

The meander pattern in figure 3-5 (a) was designed and written before the proximity-effect-correction program was developed. In this particular experiment, among other things that were wrong, the dose of the large rectangles that connect the meander to the gold contact pads was too high. Due to proximity effect, the lines at the left and right edges of the meander were overdosed while the center of the meander was under-dosed. On the other hand, the meander pattern in figure 3-5 (b) was designed after developing and using the proximity effect correction program. This meander design has a different geometry from the one designed before using PEC. This corrected meander has uniform linewidth across the active area.

Figure 3-5 is an extreme example where we simply could not get decent results by

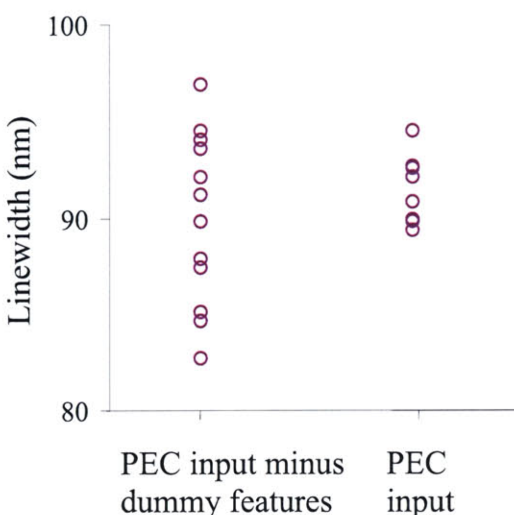


Figure 3-6: Plot of measured linewidth at strategic locations on the resultant meander for two cases.

designing an input pattern without PEC. Next, a comparison is made instead between a corrected input pattern and the same input pattern minus the dummy features.

The experimental results for both cases look qualitatively similar. However, the quantitative linewidth variation was different.

Figure 3-6 shows that without the extra dummy features, the spread in linewidths across the resultant meander was twice that of the corrected input pattern. Linewidths were measured at strategic locations of the active area where the largest variations in linewidth were expected (i.e. at the four corners, four edges and middle). A narrower linewidth variation is observed in the meander structure written using the corrected input pattern.

## 3.6 Determining the accuracy of the PEC

More accurate models for the electron beam PSF usually include an additional exponential term in the $PSF$. Even though the most direct check of PEC accuracy is by measuring the $PSF$ of the electron-beam, results obtained thus far already indicate that the PEC is accurate enough for our purposes.

To determine the accuracy of this model, a dose matrix of PEC designed meanders

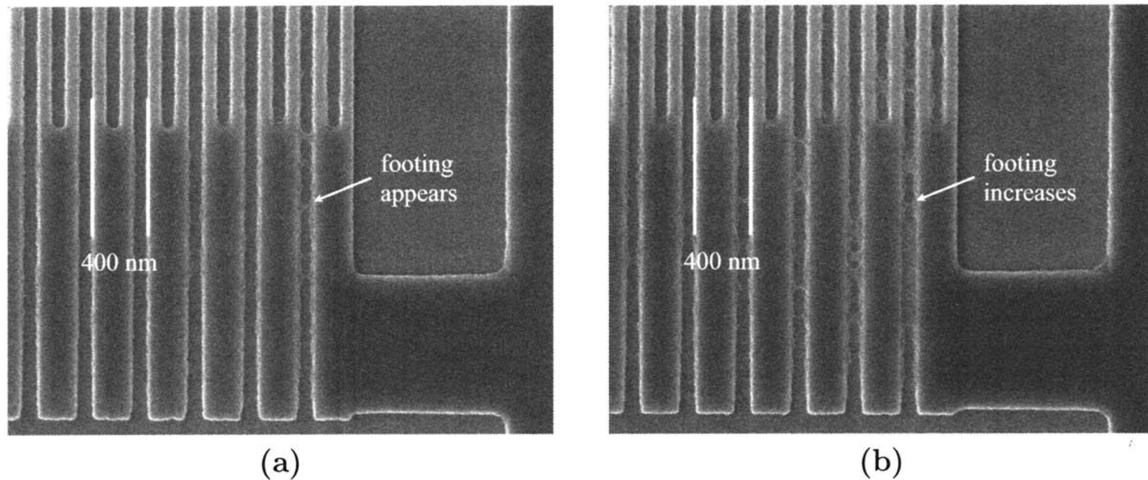


Figure 3-7: SEM image showing one corner of the meander pattern where footing begins to appear with increasing dose.

with different wire widths was written in 100 nm thick HSQ (obtained from FOx-14 diluted with MIBK at a 1:1 ratio) on sapphire substrates. The nominal linewidths of the meanders were 60 nm, 100 nm, 140 nm and 200 nm. All have 100 nm gaps between the lines.

The dose matrix for all meander patterns was written at 30 kV at a beam current of 150 pA (using a 20 $\mu$m aperture) and a step size of 4 nm and developed for 8 minutes in MF CD-26 at 18 °C. The starting dose setting was 300 $\mu C/cm^2$.

We used the PEC program to calculate the dose in the regions between meander lines. This "inter-line" dose value has to be kept below a threshold value to avoid footing between lines.

The dose matrix was analyzed in the SEM and the linewidth of each meander pattern was measured. Footing in between lines appeared as the dose increased beyond a certain point. Figure 3-7 (a) shows an example of the onset of footing. Inter-line dose at the footing was calculated to be about 97 $\mu C/cm^2$. Figure 3-7 (b) shows the same pattern as in 3-7 (a) but written using 1.1x the dose setting. Footing was seen to be more obvious at this higher dose. The calculated inter-line dose at the onset of footing was noted. This procedure was repeated for all meander designs.

We plotted in figure 3-8 the normalized linewidth (measured linewidth/ nominal linewidth) versus dose between lines. From this plot, we see that different meander

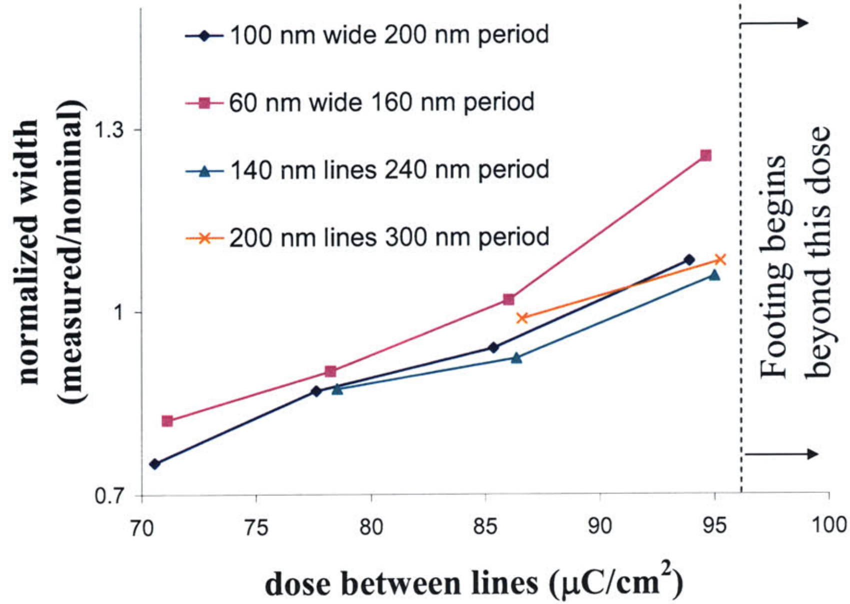


Figure 3-8: Plot of normalized linewidth versus dose in between lines for different meander designs

designs have the same onset dose, beyond which footing starts to appear. This shows that the PEC program can be used to accurately design and assign correct doses for high-density patterns.

## 3.7 Designing arbitrary meanders

Using the PEC program, several arbitrary meander patterns were designed. Figure 3-9 a) shows the successful implementation of the PEC program in designing a uniform-linewidth, large-area meander of 10 $\mu$m by 10 $\mu$m. Figure 3-9 b) is a section of a meander designed to have 100 1.3-$\mu$m-long and 100-nm-wide segments.

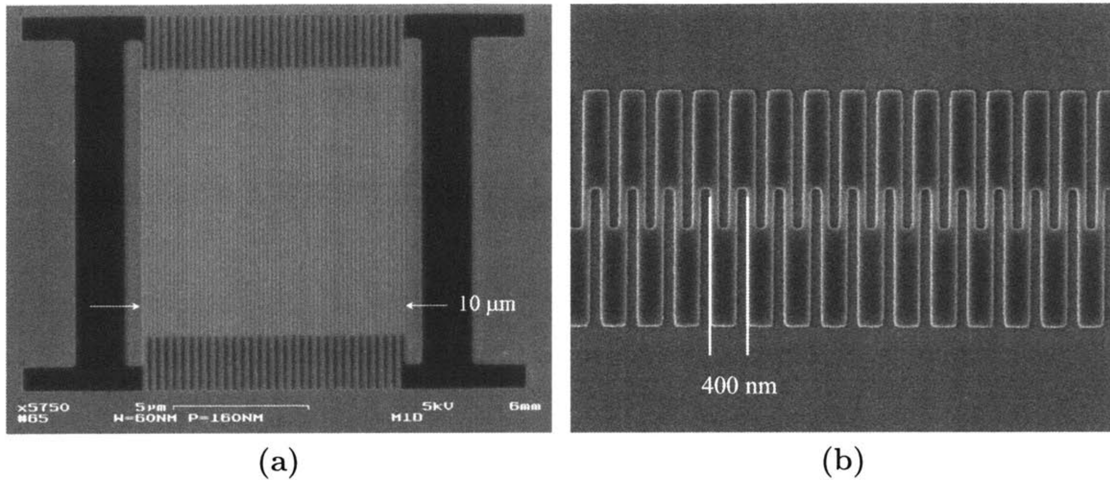


(a) (b)

Figure 3-9: SEM image of two different meander designs using the PEC program.

## 3.8 Hydrogen-Silsesquioxane (HSQ) negative-tone electron resist

### 3.8.1 Background information on HSQ

The chemical, HSQ, was first studied in 1970 by Fry and Collins [28]. Now, HSQ is commercially available from Dow Corning as the FOx (flowable-oxide) product series. It is sold in different concentrations of HSQ in methyl-iso butyl ketone (MIBK) ranging from FOx-12 (most dilute) to FOx-25 (most concentrated). As HSQ is a meta stable material with a tendency to coagulate, it has to be kept refrigerated in plastic bottles.

'Sesqui', which means three halves, refers to the hydrogen silsesquioxane chemical formula of $(HSiO_{3/2})_n$. The subscript, n, refers to the number of $HSiO_{3/2}$ monomers there are in one HSQ molecule. Typically n = 8 and the HSQ molecule has a cage-like structure [29, 30, 31] as shown in figure 3-10. However, as explained in [30], randomly structured molecules also exist in the FOx solutions in addition to the perfectly formed cage structures.

HSQ is mainly used as a spin-on interlayer dielectric in the fabrication of integrated circuits (ICs). It has the advantage over conventional plasma-enhanced chemical vapor deposited (PECVD) $SiO_2$ due to its lower dielectric constant (which is only 2.8)

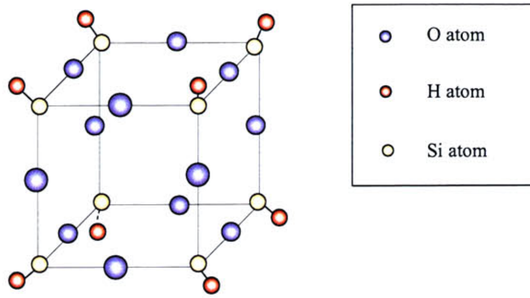


Figure 3-10: Three dimensional cage-like molecular structure of HSQ.

is compared to that of $SiO_2$ (which is 4.5). The low dielectric constant reduces the resistance-capacitance (RC) time constant in ICs and therefore increases the operating speeds of ICs.

Namatsu et al. discovered in 1998 that HSQ could also be used as a high-resolution negative-tone electron resist [19]. We found that HSQ was suitable due to its high resolution [18] and low line-edge roughness [19] therefore enabling us to define sub-100-nm nanowires with few constrictions. HSQ also has negligible absorbance at 1550 nm, allowing us to integrate HSQ into a later part of the project as the dielectric layer in an integrated optical resonator.

### 3.8.2 HSQ exposure mechanism

During electron-beam exposure, highly energetic electrons provide the activation energy to break the weak Si-H bonds and promote formation of the stronger siloxane (Si-O-Si) bonds [19]. Electron-beam irradiation thus causes resist cross-linking. This reaction converts the small cage-like structures into a long-range network structure. The conversion occurs through the opening up of the cage molecules and subsequent joining with neighboring molecules to form larger mesh-like structures. This process is illustrated in figure 3-11:

1. Two adjacent HSQ molecules are initially not crosslinked. Due to the energy from the electron beam (or a high-energy photon) one Si-H and the nearest Si-O bonds are broken (shown in red).

2. The dangling Si bond preferentially bonds with the nearest dangling O bond forming a Si-O-Si link between the two HSQ molecules. The H atom combines with H atoms from similar reactions to form $H_2$ gas.

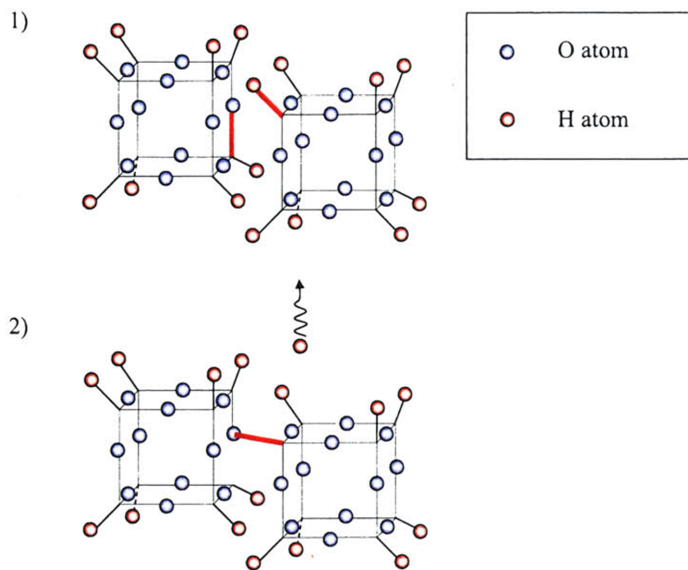


Figure 3-11: Schematic drawing illustrating a likely process that occurs during crosslinking.

The cage:network-structure ratio in the resist decreases during electron-beam exposure [32]. Therefore the high cage:network ratio in unexposed HSQ decreases during exposure due to the cage to network electron-beam induced conversion. Fourier-transform infrared spectroscopy (FTIR) measurements of the resist is often used to verify this reaction. Measurements indicate an increased amount of network structured molecules and a reduction in cage-like structured molecules after electron-beam exposure [19, 33, 32].

Figure 3-12 shows a typical FTIR absorption spectra of HSQ before and after electron-beam exposure. The figure was adapted from [19]. Notice the decrease in absorption at the Si-O cage bond stretching and Si-O cage bond bending peaks after exposure. These changes agree with our understanding that electron-beam exposure converts cage-like structures in HSQ into long range network structures.

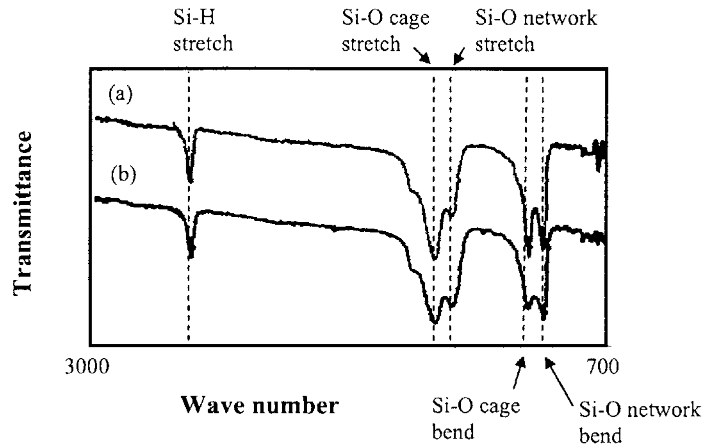


Figure 3-12: FTIR absorption spectra of a) unexposed HSQ resist and b) e-beam exposed HSQ resist. The figure was adapted from [19].

Another argument that crosslinking occurs due to the breaking of S-H bonds and the formation of Si-O-Si bonds is as follows. In order for crosslinking to occur, one Si-H bond and one Si-O bond has to be broken as shown in figure 3-11. Hence an activation energy is needed to simultaneously break one Si-H and one nearby Si-O bond. The bond energies between H-H, Si-H and Si-O are as follows:

1. Si-H bond energy = 318 kJ/mol

2. Si-O bond energy = 452 kJ/mol

3. H-H bond energy = 432 kJ/mol

The activation energy required is therefore roughly equal to (318 kJ + 452 kJ)/$N_A$ = 8 eV where $N_A$ is the Avogadro number. This value agrees well with the experimental results of Peuker et al. in [34] where HSQ crosslinking can also be induced by 157 nm wavelength light but not by 193 nm wavelength light. The energy of a single photon of light at 157 nm wavelength is evaluated to be 7.9 eV which is very close to the above rough calculation of the activation energy.

### 3.8.3 HSQ development mechanism

Development occurs via ionization by bond scission and not by dissolution [19]. No information can be found in literature on the actual chemical reactions that occur during HSQ development. However, experiments by van Delft [31] suggest that the development process occurs due to the hydroxide ions ($OH^-$) in the developer. This is consistent with the observation that both TMAH and KOH solutions are able to develop HSQ as both contain $OH^-$ ions. Figure 3-13 illustrates a possible chemical reaction that occurs during development:

1. Ionization begins when $OH^-$ ions approach the Si-H bonds.

2. Substitution reaction occurs leading to the breaking of Si-H bonds and the formation of stronger Si-O bonds.

3. H radicals recombine to form $H_2$ gas.

4. When all the H atoms have been substituted with $OH^-$ ions, the modified HSQ molecule is now ionized and can be carried away by the $(CH_3)_4N^+$ ions and water molecules.

Using the bond energies listed in section 3.8.2, we can calculate that the development process is energetically favorable.

### 3.8.4 Process details, experiments and results

HSQ is not an easy electron resist to work with compared to the conventional polymethylmetacrylate (PMMA) positive tone resist due to HSQ's lower contrast and poor adhesion with NbN. Furthermore, HSQ is sensitive to spin-coating-to-exposure and exposure-to-development delays [31]. In this project, spin coating, exposure and development were done within 24 hours to achieve reproducible results. We were able to get good results with HSQ after developing the following process:

1. Clean samples by rinsing in acetone followed by DI water. Blow samples dry using a $N_2$ gun.

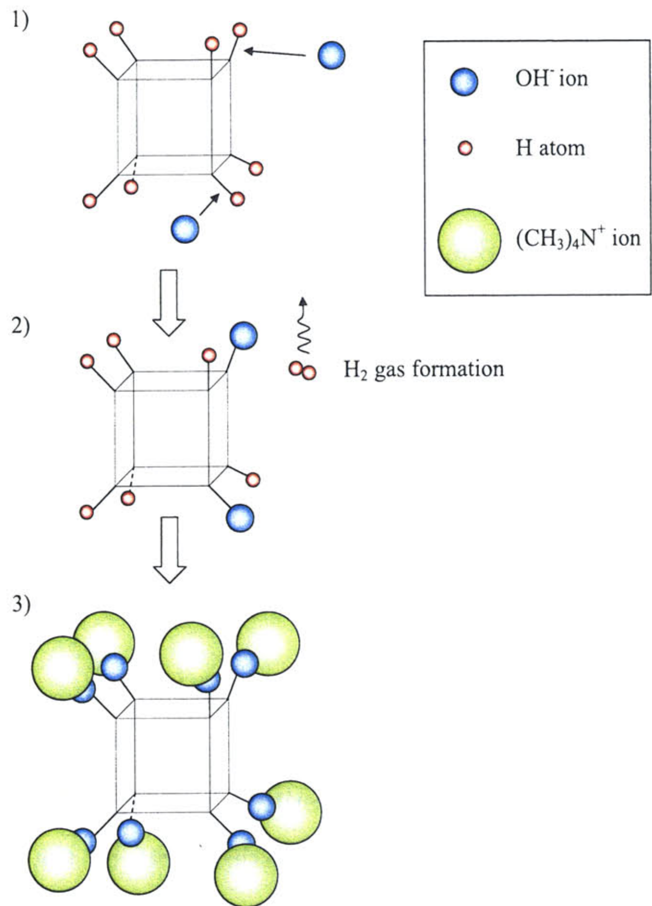


Figure 3-13: Cartoon drawing showing the possible reactions that occur during HSQ development.

2. Spin coat FOx-14 diluted in MIBK in a 1:1 ratio onto samples to a thickness of 100 nm.

3. Bake on hot plate at 90 °C for 3 minutes.

4. Expose patterns in Raith 150 EBL at 30 kV using 4 nm step size and magnification range 2.

5. Develop in Shipley Microposit MF CD-26 TMAH developer for 8 minutes. Development temperature is roughly 18 °C.

6. Rinse in DI water.

7. Blowdry using $N_2$ gun.

Nanowires with linewidths in the order of 50 - 200 nm were routinely written in the HSQ resist using EBL. Hence a resist thickness of 90 nm was suitable for this application. This resulted in narrow features with an aspect ratio (height/width) of less than 2. This aspect ratio is low enough to prevent feature collapse without requiring a post-develop supercritical drying process.

E-beam exposure was done at 30 kV to achieve the highest attainable resolution of the Raith 150. It is important that magnification range 2 is used to expose the patterns. The magnification range determines the type of digital to analog converter (DAC) used to control the electron-beam X and Y deflectors. A low-resolution/noisy DAC is selected in magnification range 1 resulting in rough/squiggly lines while a high-resolution/low-noise is used in magnification range 2. Figure 3-14 shows the difference between exposures done using magnification range 1 (figure 3-14 a) and magnification range 2 (figure 3-14 b).

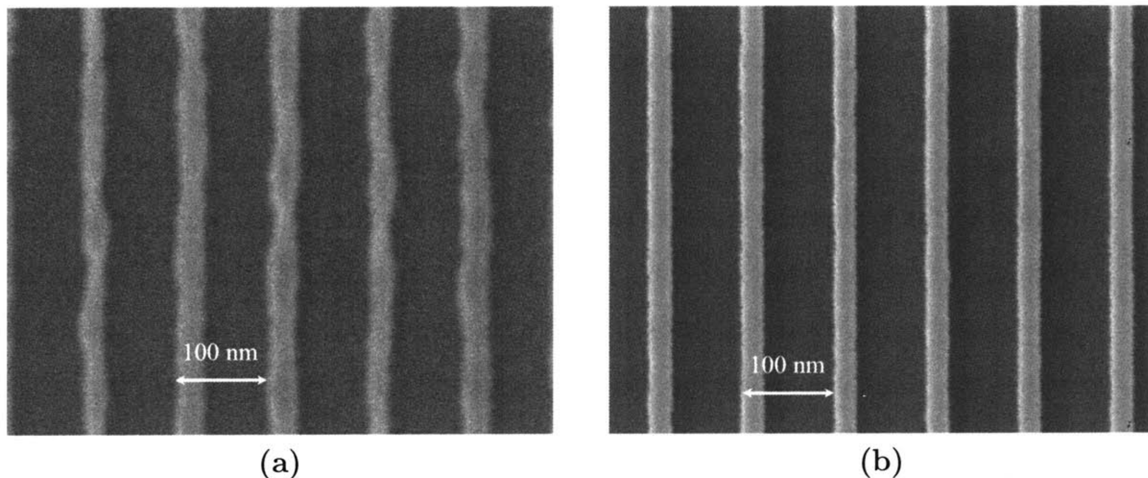


Figure 3-14: SEM images of gratings written using magnification range 1 (figure a) and magnification range 2 (figure b) settings on the Raith 150.

### 3.8.5 HSQ contrast

Baking HSQ at elevated temperatures (e.g. 220 C) results in poor resist contrast because it promotes cross-linking in the resist [32]. Baking at high-temperatures re-

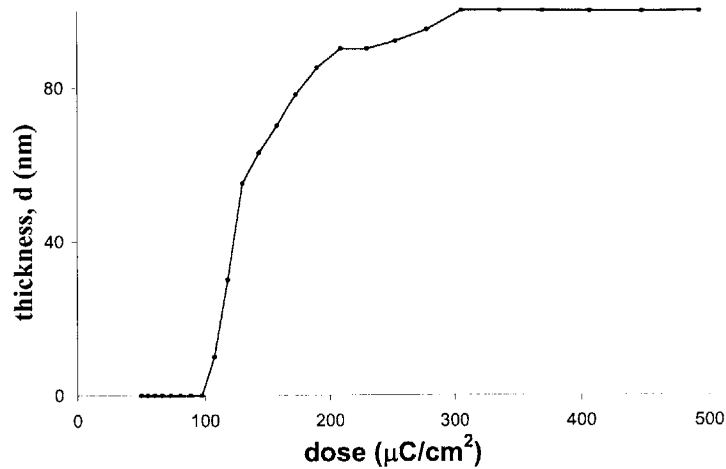


Figure 3-15: Contrast curve for 90 nm thick HSQ written at 30 kV and 4 nm step size using different concentration of developers.

duces the cage:network ratio in the resist and effectively acts as a blanket background dose, therefore reducing the contrast. Thus, one would want to have as little network formation as possible in the unexposed resist in order to maximize contrast.

Baking the resist at 90 °C for 3 minutes resulted in better contrast compared to baking at 150 °C for 2 minutes followed by 220 °C for 2 minutes. Figure 3-15 shows the contrast curve using the 90 °C 3 minute bake for diluted FOx-14. The contrast curve was obtained by exposing 10 $\mu$m by 10 $\mu$m square areas at gradually increasing doses in the Raith at 30 kV acceleration voltage and 4 nm step sizes. Rectangles exposed using different step sizes, with the same dose settings will have different *actual* doses.

After developing the sample in Shipley Microposit MF CD-26, the remaining thickness of HSQ is measured using a Digital Instruments atomic force microscope. The onset dose for HSQ is about 97 $\mu$C/cm$^2$. This value was used to calibrate the PEC program in section 3.6. During meander SN-SPD designs, the calculated inter-line doses have to be kept below this value to avoid footing.

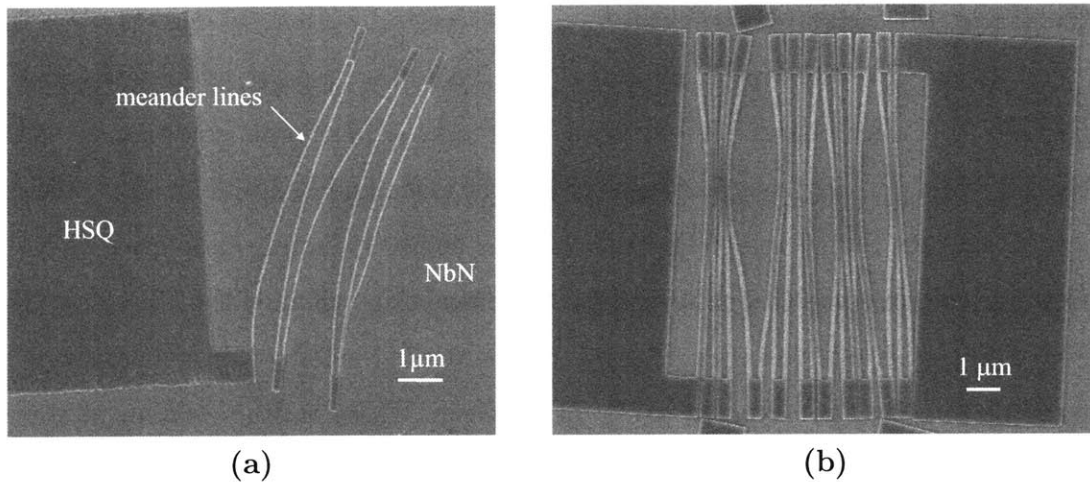


(a) (b)

Figure 3-16: SEM image showing HSQ structures that have peeled off the NbN surface and shifted from its original position after development.

### 3.8.6 Adhesion problems

Adhesion between HSQ and silicon substrates with unremoved native oxide is generally good. However, we observed adhesion problems between HSQ and the epitaxial layer of superconducting NbN when samples were developed for 1 hr. One quick solution to this problem was to reduce the development time from one hour to only 8 minutes. Unexposed HSQ spun onto a Si wafer was found to be completely developed away in less than one minute. Hence, the long development of 1 hr was unnecessary.

Figure 3-16 shows what happens when the HSQ structures detach from the NbN surface and are displaced from their original position. Figure 3-16 a) shows a severe case of detachment where the structures completely peel off and tear away. In less severe cases, figure 3-16 b), capillary forces, which exist during blow drying, cause the closely spaced lines to detach from the surface and stick to each other.

### 3.8.7 HSQ and NbN wettability experiments

To study the HSQ-NbN adhesive forces, we tested the hydrophilic or hydrophobic nature of NbN and HSQ.

A drop of DI water was placed on the surface of the NbN films prior to any processing. The water droplet does not wet the surface, and a contact angle between

the droplet surface and wafer surface was observed to be about 40 degrees.

In a separate experiment, we found that NbN film becomes hydrophilic after a 5 minute UV ozone clean. It is possible that a layer of organic contaminant coats the NbN film, making it hydrophobic before the clean and hydrophilic after. We did not investigate the effects of the clean on the superconducting properties of NbN. However, we observed that an overnight UV ozone clean thinned the NbN film. The NbN film on this sample appeared more transparent in a side-by-side comparison with a sample that was not exposed to UV ozone clean. Therefore the cleaning step may cause damage to the film.

To test the hydrophilic nature of HSQ, HSQ was spun onto a Si wafer to a thickness of ~ 100 nm and baked at 150 °C for 10 minutes on a hot plate. The long bake at 150 °C was to ensure the complete evaporation of the organic solvent, MIBK, which has a boiling temperature of ~ 116 °C. HSQ was found to be very hydrophobic. Water droplets make a contact angle of about 90 degrees and would simply slide off the surface of the HSQ-coated wafer.

The hydrophobic nature of HSQ is due to the absence of any net polarity in its cage-like molecular structure. Additionally, the Si-H bonds (similar to the organic C-H bonds) are only slightly polar, thus contributing to the overall hydrophobic nature of HSQ. After ashing the HSQ coated wafer in an asher for 5 minutes (at settings of 100 W power, 400 mTorr pressure and 20 % $O_2$ 80 % Helium plasma composition) we observed that the surface of HSQ becomes hydrophilic. The oxygen plasma in the asher converts the top surface of HSQ into predominantly $SiO_2$, making it hydrophilic.

As both HSQ and NbN (without UV ozone cleaning) are hydrophobic, the main force of attraction between them is the weak van der Waals force. This weak attraction results in poor adhesion between HSQ and NbN. In fact, a hydrophilic film would probably adhere just as well to a hydrophobic surface as a hydrophobic film would.

### 3.8.8 Solving adhesion problems

Adhesion between HSQ and NbN improves by increasing exposure dose and shortening development time. The maximum exposure dose that can be used to expose

the SN-SPD pattern is determined by setting the inter-line dose to be $\lesssim$ HSQ onset dose. Hence the maximum exposure dose for the meander lines is the maximum dose that does not cause footing. Similarly, the minimum development time is the shortest time needed to completely remove any inter-line resist.

Adhesion improves with increasing dose possibly due to the following reason. First of all, we know that the developer reacts with Si-H and not Si-O bonds. We now focus at the reactions that occur at the HSQ-NbN interface during development. Lightly exposed HSQ will have a higher concentration of Si-H and a lower concentration of Si-O bonds at the interface compared to heavily exposed HSQ. The higher concentration of Si-H bonds in lightly exposed HSQ causes a higher developer penetration rate at the HSQ-NbN interface. This developer penetration leads to resist detachment.

On the other hand, the developer penetration rate is lower in heavily exposed HSQ. By reducing the development time, we improve adhesion by avoiding complete developer penetration at the interface. Hence, highly exposed HSQ sticks well to NbN while lightly exposed HSQ tends to detach from the surface. Exposure dose and development time have to be well controlled in order to achieve good adhesion while still clearing in between lines. This makes the fabrication of single wires easier than densely packed meander structures as we are not concerned with footing in the former.

## 3.9 Reactive ion etching

In the final fabrication step, the pattern was transferred into the NbN film via reactive ion etching (RIE) using HSQ as the etch mask. Etching conditions were as follows:

1. Gases = $CF_4$ + $O_2$ at a flow rate of 15 standard cubic centimeter per minute (sccm) and 1 sccm respectively,
2. Pressure = 20 mTorr,
3. DC bias = 116 V,
4. Power = 54 W.

The low DC bias setting was used to reduce plasma-induced damage to the NbN film.

The NbN etch rate at these conditions was roughly 2 nm/minute. HSQ was etched away at a higher rate of $\sim$ 18 nm/minute. The thickness of HSQ after the etch was about 50 nm. This thinned layer of HSQ was not removed from the surface of the completed SN-SPD.

Figure 3-17 shows a meander pattern that was transferred into NbN via RIE. We took advantage of the high image contrast between the conductive NbN and the non-conductive sapphire substrate to check the continuity of the nanowire. Charge build-up on the non-conductive sapphire caused a bright outline around the conductive NbN wire.

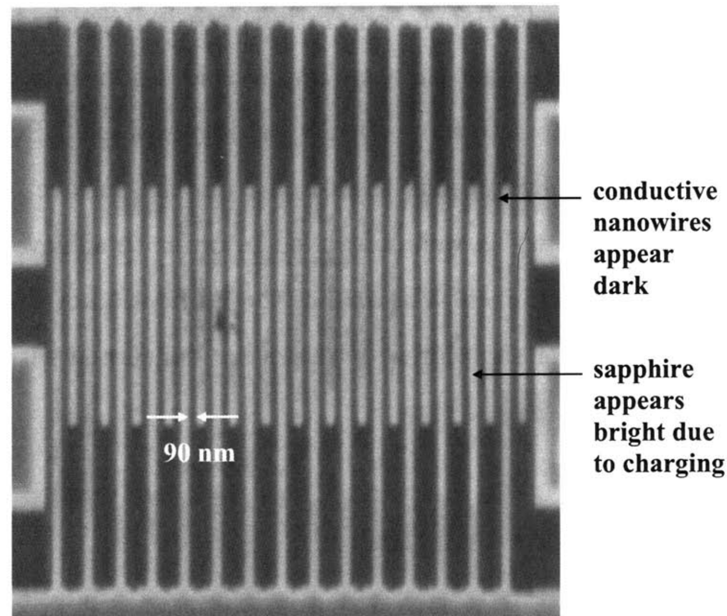


Figure 3-17: SEM image of a meander pattern after RIE.

Figure 3-18 is an example of a discontinuous nanowire after RIE. HSQ was less than 40-nm thick at several places on the meander before the etch. In these regions HSQ did not act as a good etch-mask causing the underlying NbN to be etched away and damaged. Therefore, the HSQ thickness after development has to be at least $>$ 50 nm to successfully transfer the pattern into NbN.

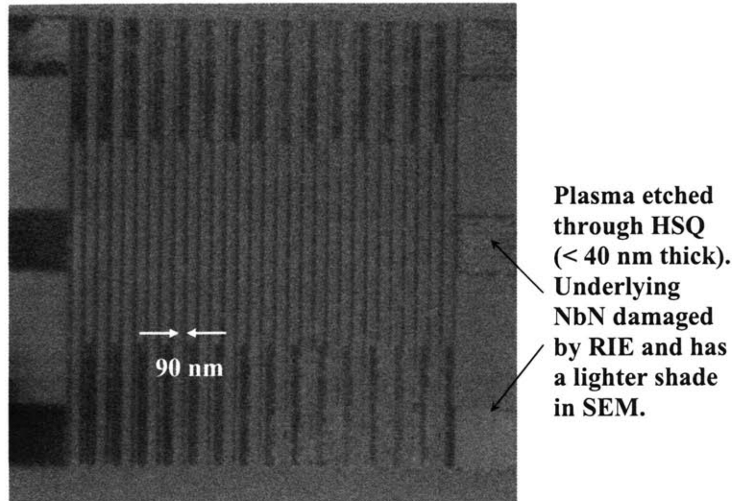


Figure 3-18: SEM image of a damaged meander pattern after RIE.

## 3.10 Material damage

No supercurrent was observed in the first several batches of samples that we made. Instead, we saw series resistances > 10 kΩ that switched several times to even higher resistances in steps of about 10 kΩ as the current is increased beyond $I_c$. We believe that this effect occurred because the NbN films were damaged by plasma during RIE and/or excessive heat.

As a result of the damage, portions of the wires were damaged leaving some other portions superconducting. This explains the large series resistance (due to damaged portions) as well as the step-like switching (due to superconducting portions).

### 3.10.1 Plasma-induced damage

We observed physical plasma damage at high DC bias settings of 375 V. Figure 3-19 shows one particular situation where the sample was damaged after RIE. The explosion marks at the four corners could be caused by plasma arcing from one side of the meander to the other to bypass the resistive meander in between. This meander was made using an earlier process where PMMA instead of HSQ was used as the electron resist.

We solved this problem by reducing the reactive ion etching DC bias setting from

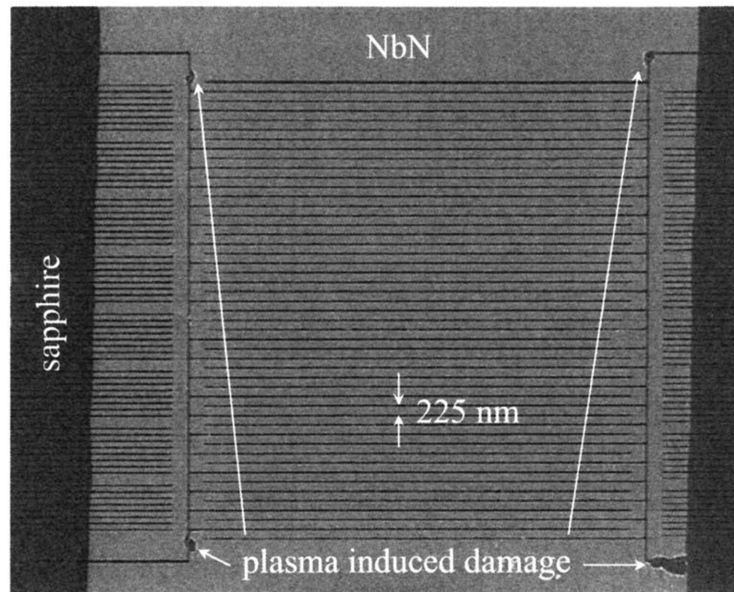


Figure 3-19: SEM image of a meander pattern with plasma induced explosion marks at the four corners.

375 V to 116 V. This reduction resulted in a gentler etch condition and prevented plasma arcing.

### 3.10.2 Thermal damage

Unfortunately, the samples made under the gentler etching conditions were still not superconducting. We discovered that the samples were damaged when they were heated to 160 °C in air to melt indium foil between the sample and probe-station stage during sample mounting. After switching to silver paint to mount samples, we started observing superconductivity in the nanowires.

In a separate experiment we found that the samples could be heated to at least 200 °C in vacuum without damaging the nanowires. This strongly suggests that elevated temperatures in air will damage the nanowires by oxidizing NbN.

### 3.10.3 Chemical damage

We tried removing HSQ after etching by immersing the sample for 2 minutes in a diluted solution of one part buffered oxide etch solution ($NH_4F$ - HF) to five parts DI

water. The nanowires (which were tested to be superconducting before the treatment) were no longer superconducting after the treatment.

The standard RCA cleaning process, a 5:1:1 ratio of $H_2O$:$H_2O_2$:$NH_4OH$ solution at 75 °C, was found to completely dissolve NbN just after 10 s.

## 3.11 Summary

Process details for fabricating nanowires for SN-SPDs were presented. This process uses EBL exposure of a negative-tone electron resist, HSQ, followed by pattern transfer via reactive-ion etching using HSQ as the etch mask. A proximity-effect-correction program was developed and used to achieve uniform linewidths in the SN-SPD meanders. Information on HSQ characteristics and possible reaction mechanisms were presented. Finally, an investigation of device damage due to sample handling and processing was presented.

# Chapter 4

# Electrical and optical testing of SN-SPDs

SN-SPDs were tested for their functionality and performance as single-photon detectors. After ensuring that the devices sustained no process-related damage, we tested the single-photon response of the detectors. For our best device we measured a detection efficiency of $\sim 10$ % at 1064 nm photon wavelength at 2.1 K and a photon-induced volage pulse duration of $\sim 3$ ns. We found that the device speed was limited by the kinetic inductance of the nanowires.

## 4.1 Cryogenic DC measurements

Cryogenic DC measurements were done as a first check of device functionality. The objective was to test the superconductivity of the fabricated nanowires by measuring their non-negligible critical supercurrent values, $I_c$. This test confirmed that the fabrication process preserved the superconductivity of NbN.

### 4.1.1 Experimental setup

DC measurements were conducted in Professor Rajeev Ram's laboratory using a cryogenic probing station from Desert Cryogenics (now a division of Lake Shore Cryotron-

ics). The probe station provided the advantage of testing multiple devices without having to wire-bond every single device to external leads. Having a large number of devices on a single sample helped us eliminate differences in devices due to process variations. Recently, we have made 8-mm-by-8-mm samples with as many as 154 devices on each.

A HP 4156B semiconductor parameter analyzer was used to obtain the voltage versus current ($I$-$V$) characteristics of the nanowire. With the parameter analyzer in the current-bias mode, current (in increasing steps) was passed through the nanowire and the corresponding voltage across the terminals was measured.

A bias tee model 5541A from Picosecond Pulse Labs was used as a filter to reduce the noise from the parameter analyzer. We observed that noise suppressed $I_c$ so the bias tee allowed us to measure the highest possible values of $I_c$.

Samples were stuck onto the probe-station stage using silver paint, providing good thermal contact between sample and stage. The probe station chamber had a thermal radiation shield and was vacuum pumped using a Varian V-70 Turbo pump cart, with a DS 102 backing pump. High vacuum was necessary to provide good thermal insulation from the external environment and to avoid air condensation onto the sample surface during cooling down to 4.2 K.

Liquid helium was transferred from a 100 L dewar to flow through the probe station cooling conduits, cooling the stage down to 4.2 K (the boiling temperature of liquid helium). As liquid helium flowed through the system it cooled the stage and thermal shields and finally exited the system through an exhaust. The probe arms were well thermalized to the shield temperature (which was $< 15$ K). The temperature of the stage could be lowered to 1.5 K by pumping on the helium bath under the stage.

## 4.2 DC measurement results

We measured $I$-$V$ for a single wire over a range of temperatures. From the $I$-$V$s, we studied the temperature dependence of $I_c$ and normal state resistance.

### 4.2.1 *I-V* characteristics

*I-V* characteristics for a 100-nm-wide nanowire at a range of different temperatures is shown in figure 4-1. The horizontal portion of the trace (from 0 to $I_c$) represents the region of the *I-V* where the current flows without resistance. For a particular temperature, $T$, this supercurrent flowed up to a critical current $I_c(T)$. Above $I_c(T)$, the wires became resistive and the *I-V* trace follows that of a normal resistor. Hence, the wire can be thought of as a variable resistor that switches from zero resistance, below $I_c(T)$, to almost 90 kΩ above $I_c(T)$.

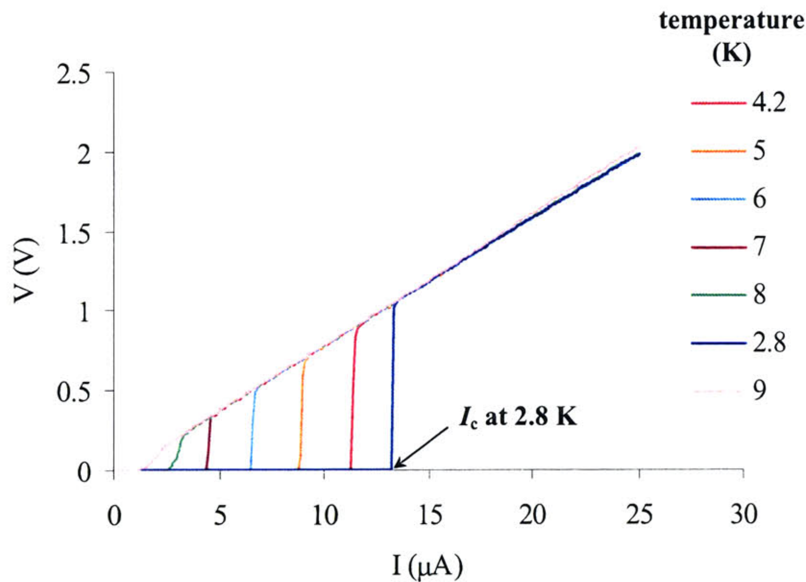


Figure 4-1: Plot of V vs I for a 100 nm nanowire at different temperatures.

### 4.2.2 Problems with electrical contact during DC measurements

We occasionally encountered difficulty in making good electrical contact with the sample gold pads during cryogenic testing. This problem was probably due to a film of insulating condensation that built up on the sample surface (which was the coldest surface in the chamber) during testing at low temperatures. Whenever this happened, we lifted the probe tips off the sample and heated the sample stage up to about 100

K for a minute before cooling it back down. Doing so desorbed the insulating film and re-established good electrical contact between probe tips and sample pads.

### 4.2.3 $I_c$ dependence on temperature

Figure 4-2 shows how $I_c$ changes with temperature, $T$. As the temperature was increased, $I_c$ decreased down to zero at $T_c$, above which the wire was no longer superconducting.

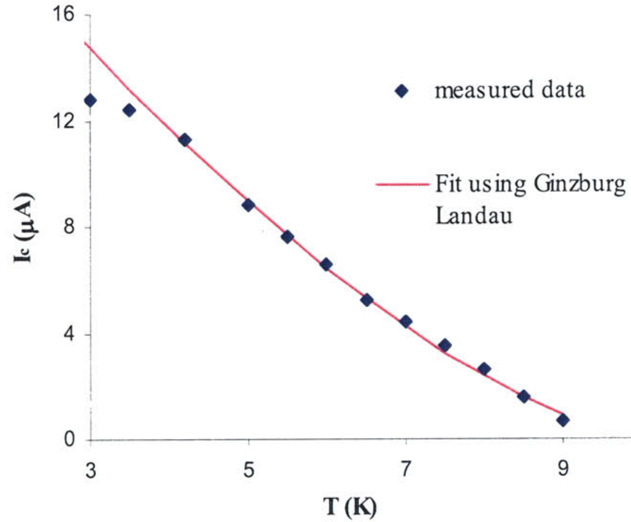


Figure 4-2: Plot of $I_c$ vs T for a 100 nm nanowire.

Equation (4.1) below, which was derived from Ginzburg-Landau theory, fits the temperature dependence of $I_c$ data reasonably well at temperatures close to $T_c$ [35].

$$I_c(T) = I_c(0)(1 - (\frac{T}{T_c}))^{3/2} \tag{4.1}$$

This equation was derived by calculating the maximum current that can flow in a wire before the magnetic field that it generates exceeds the critical magnetic field of the superconductor. A more involved model would probably fit our measured data more accurately over the entire temperature range. However we have not yet fully modelled the mechanism that determines the critical current in a nanowire.

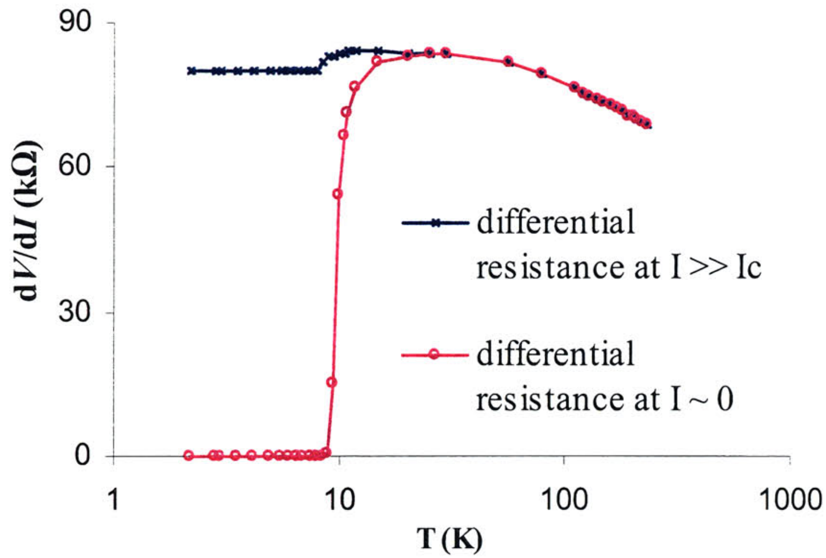


Figure 4-3: Plot of R vs T for a 100 nm nanowire.

### 4.2.4 Resistance temperature dependence

Figure 4-3 shows the change in differential resistance with temperature. In the plot of differential resistance (measured at $I >> I_c$) versus $T$, it is interesting to note that the normal state resistance at $T < T_c$ is very close to being constant and also that there is a bump upwards towards a maximum differential resistance at $T_c$. The resistance of the wire decreases with increasing temperature beyond $T_c$. We suspect that this decrease in $R$ with $T$ could be a characteristic of thin superconducting films. $T_c$ is defined as the temperature when the differential resistance (measured at $I$ 0) is 1 % of maximum. The $T_c$ value of our nanowire is about 9.6 K.

### 4.2.5 $I_c$ and conductivity dependence on wire width

In a separate experiment, several nanowires of different widths were fabricated on the same sample. Nanowire widths of 50 nm, 100 nm, 200 nm and 400 nm were tested in a separate setup in Professor Terry Orlando's laboratory. In this setup, the sample was wirebonded to a cryogenic dip probe and dunked into a liquid helium dewar to cool it down to 4.2 K.

$I$-$V$ characteristics were obtained using an oscilloscope and a function generator.

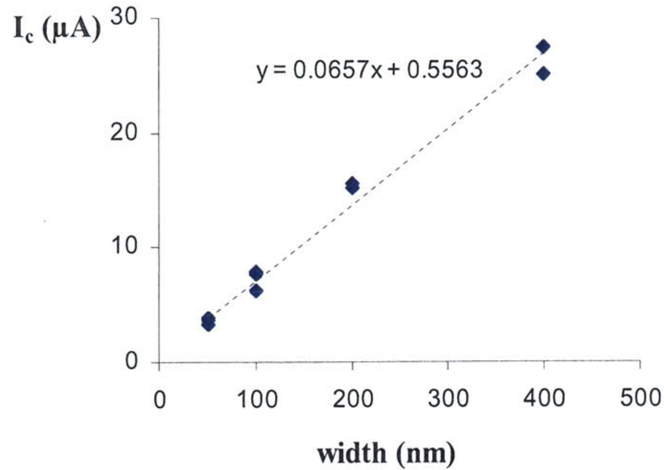


Figure 4-4: A plot of $I_c$ versus wire width. All wires were 5 $\mu$m long.

For the same wire width, the measured critical currents using this setup was lower than the measurements using the parameter analyzer and probe station due to the lack of noise filtering. Trends of $I_c$ and normal state conductivity versus wire width are obtained as shown in figure 4-4 and 4-5 respectively.

The conductivity was measured from the $I$-$V$ characteristics at $I$ values $>> I_c$. The linear trends are expected as the critical currents and conductivities are directly proportional to the wire cross-sectional area. By using the slopes of the linear trends, the sheet resistance of the 4-nm-thick NbN film was calculated to be $\sim$ 600 $\Omega$/square and the critical current density, $j_c \sim$ 2 MA/cm$^2$.

## 4.3 High-speed tests

### 4.3.1 Experimental setup

High-speed tests were conducted in Lincoln Laboratory using a similar cryogenic probe station as the one in Professor Rajeev Ram's laboratory with the addition of a high-speed oscilloscope and RF amplifiers. The experimental setup is shown in figure 4-6.

The setup included the following components:

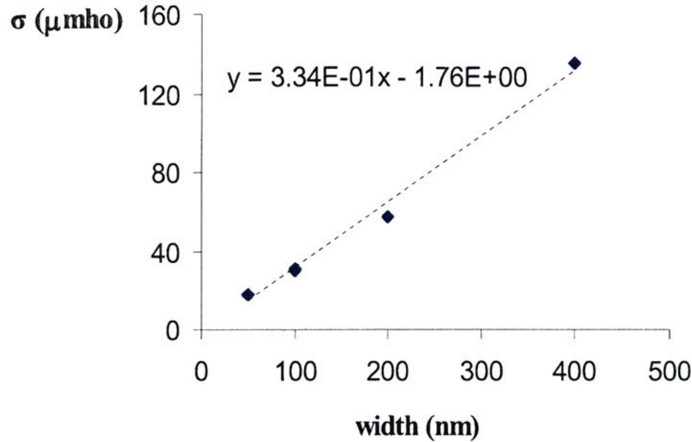


Figure 4-5: A plot conductivity versus wire width. All wires were 5 $\mu$m long.

1. A Picosecond Pulse Labs model 5541A bias tee (inductance value of 1 mH , capacitance of 0.02 $\mu$F, bandwidth of 80 kHz to 26 GHz)

2. Two cascaded ZJL-3G Mini-Circuits RF amplifier (each with a bandwidth of 20 MHz to 3 GHz and a gain of 18 dB)

The bias tee allows DC biasing through the inductor and directs high frequency response signals through the capacitor. The current source is battery powered to reduce noise and was built at Lincoln Laboratory using a low-noise zener-diode voltage-reference, a potentiometer and an op-amp as the main components. In figure 4-6, the SN-SPD was modeled as an inductor in series with a resistor and switch in parallel. This SN-SPD model will be explained in section 4.4.

We tested the photon response of the SN-SPD at two different wavelengths. A Calmar Optcom femto-second pulsed laser source was used for 1550 nm wavelength and a fast switched diode laser was used for 1064 nm wavelength. Light was fiber-coupled into the probe station through a tapered/lensed tip fiber from Oz Optics. The fiber tip focused the light to a spot size of approximately 15 $\mu$m in diameter at the detector active area.

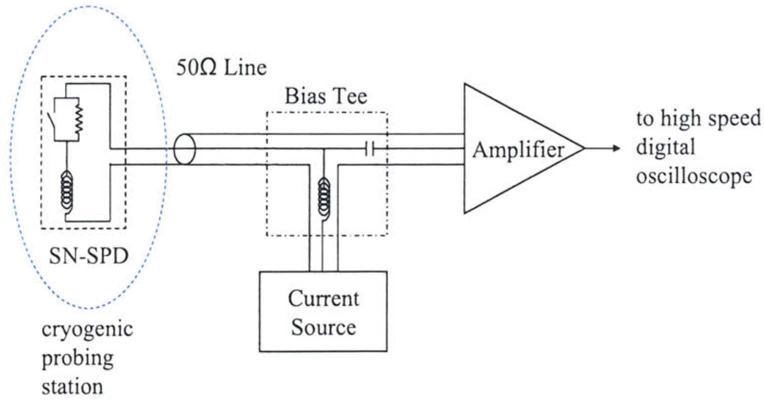


Figure 4-6: Circuit schematic for high-speed experimental setup.

### 4.3.2 High-speed test results

Figure 4-7 shows a pulse shape of a 100 nm wide, 6 $\mu$m by 8 $\mu$m active area SN-SPD meander. The pulse duration was on the order of several nanoseconds.

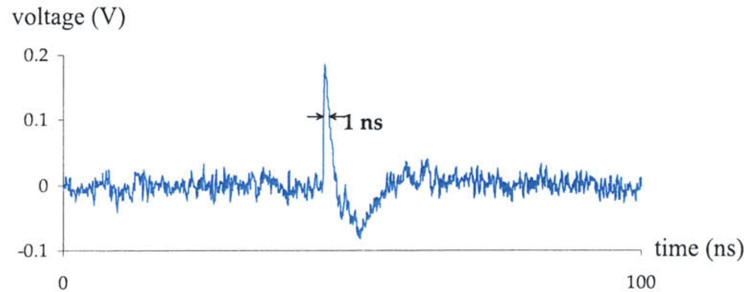


Figure 4-7: Voltage pulse measured at the high speed oscilloscope of the SN-SPD response to an absorbed single photon.

We measured the detection efficiencies of the devices at temperatures of 2.1 K and 4.22 K and photon wavelengths of 1064 nm and 1550 nm. Figure 4-8 shows the measurement results of our best device to date which is a 6-$\mu$m-by-4-$\mu$m meander with 100-nm-wide wires and 50 % fill factor.

The observed increase in detection efficiency with decreasing photon wavelength was probably due to the larger hotspot formed by a more energetic photon. A larger hotspot should cause a larger increase in current density around the hotspot, therefore increasing the probability for a detection event.

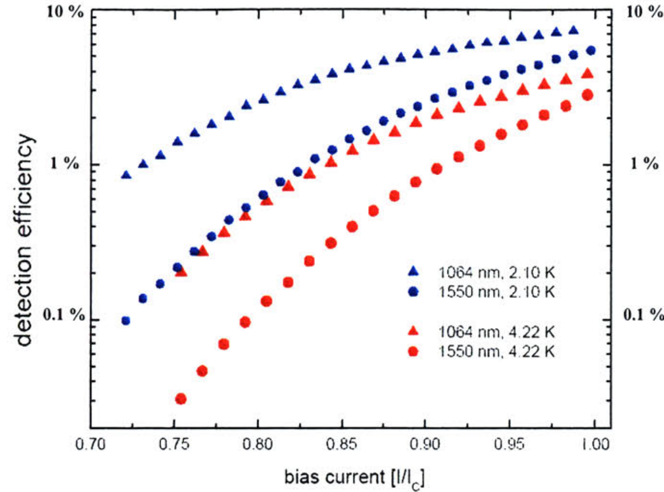


Figure 4-8: Plot of detection efficiency for single photons against bias current for photon wavelengths of 1064 nm and 1550 nm and temperatures of 2.1 K and 4.22 K.

### 4.3.3 Single-photon detection

The purpose of this experiment was to see if the SN-SPD was actually detecting single photons. In order to do this, the output from the Calmar Optcom femto second pulsed laser was attenuated so that there was less than a single photon per pulse on average. The source had a repetition rate of 10 MHz. The detector count rate versus laser power were plotted on a log scale. We can tell if the detector was actually detecting single photons by looking at the slope of the plot. Figure 4-9 shows such a plot for a 6-$\mu$m-by-4-$\mu$m meander with 100-nm-wide wires. The slope of unity shows that the detector was in the single photon detection regime.

In order to understand why this was so, we can think of the photon detection as a Poissonian process. The Poisson distribution can be derived from the binomial distribution as follows. Equation (4.2) is the probability, $P(m|N)$, of getting $m$ successes in $N$ trials given the probability of success is $p$.

$$P(m|N) = \frac{N!}{m!(N-m)!}p^m(1-p)^{N-m} \tag{4.2}$$

$$n = Np = \text{expected number of successes in N trials} \tag{4.3}$$

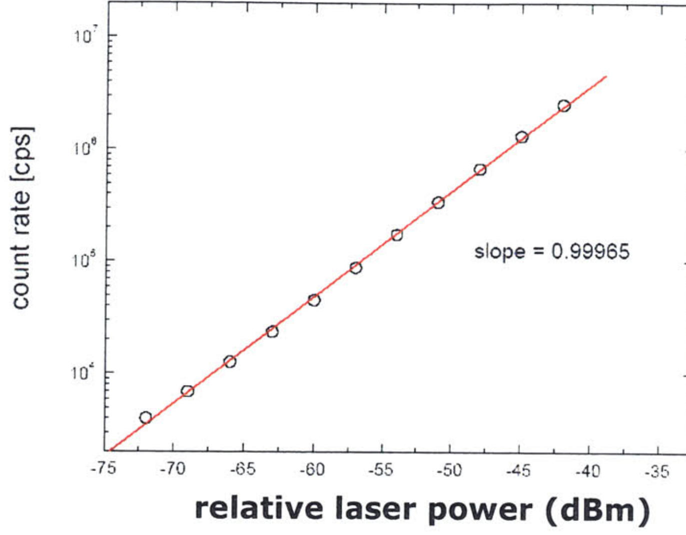


Figure 4-9: Plot of detector counts per second vs laser power.

In the limit where $p << 1$ and $N \rightarrow \infty$, we get the Poisson distribution as derived below:

$$
\begin{aligned}
P_n(m) &= \lim_{N\rightarrow\infty} \frac{N!}{m!(N-m)!}(\frac{n}{N})^m(1-\frac{n}{N})^N(1-\frac{n}{N})^{-m} && (4.4) \\
&= \lim_{N\rightarrow\infty} \frac{N(N-1)..(N-m+1)}{N^m}(\frac{n^m}{m!})(1-\frac{n}{N})^N(1-\frac{n}{N})^{-m} && (4.5) \\
&= 1 \cdot \frac{n^m}{m!} \cdot e^{-n} \cdot 1 && (4.6) \\
P_n(m) &= \frac{n^m}{m!}e^{-n} && (4.7)
\end{aligned}
$$

Equation (4.7) is the probability of getting exactly $m$ successes when the average number of success is $n$. We can use Poisson distribution to describe the photon detection process by making the following associations:

$$
\begin{aligned}
N &= \text{number of photons per pulse} && (4.8) \\
m &= \text{number of detected or absorbed photons per pulse} && (4.9) \\
p &= \text{detection efficiency} && (4.10) \\
n &= Np = \text{average number of detected or absorbed photons per pulse} && (4.11)
\end{aligned}
$$

The probability of detecting a pulse, $P_{detection}$, is equal to 1 minus the probability of not detecting any photons, $P(0)$.

$$P_{detection} = 1 - P(0) \tag{4.12}$$

$$P(0) = \frac{n^0}{0!}e^{-n} = e^{-n} \tag{4.13}$$

$$P_{detection} = 1 - e^{-n} \tag{4.14}$$

Equation (4.14) does not tell us if the SN-SPD response is actually due to a single photon as it only tells us the probability that a pulse (which may contain more than one photon) is detected. However, when the laser power is attenuated until there is less than one photon per pulse on average ($N < 1$) we have a higher certainty that the SN-SPD response is due to single photons because the probability of the detection due to a single photon $P(1)$ is greater than $P(2)$ as shown below.

$$n << 1 \tag{4.15}$$

$$P(1) = \frac{n^1}{1!}e^{-n} \approx Np \tag{4.16}$$

$$P(2) = \frac{n^2}{2!}e^{-n} \approx \frac{(Np)^2}{2} \tag{4.17}$$

$$P(1) >> P(2) >> P(3)... \tag{4.18}$$

$$\tag{4.19}$$

For example, with a detection efficiency, $p$, of 1 %, and $N = 1$, the probability of a detection event due to a single photon is 200 times greater than the that due to

two photons. Finally we can relate $N$ to *count rate* and *laser power* as follows:

$$\begin{aligned}
R &= \text{laser repetition rate} = 10^6 && (4.20)\\
count\ rate &= P_{detection} \cdot R && (4.21)\\
\log(count\ rate) &= \log(P_{detection}) + \log(R) && (4.22)\\
&= \log(N) + \log(p) + \log(R) && (4.23)\\
&= \log(N) + \text{constants} && (4.24)\\
laser\ power &= R \cdot N \cdot \text{photon energy} && (4.25)\\
\log(laser\ power) &= \log(N) + \log(R) + \log(\text{photon energy}) && (4.26)\\
&= \log(N) + \text{constants} && (4.27)\\
& && (4.28)
\end{aligned}$$

From equation (4.24) and (4.27) we see that a plot of log(*count rate*) versus log(*laser power*) will have a slope of unity when the SN-SPD is detecting single photons. At higher values of $N$ and at low bias currents, two-photon events will dominate and we would expect a slope of 2 [8].

## 4.4 Device modeling

### 4.4.1 Hotspot model

The photo-induced hotspot model presented in [16] predicts that the hotspot decays over a time-scale in the order of $\sim$ 80 ps. Figure 4-10 is a Matlab simulation based on the parameters in [16]. It shows the decay rate of quasiparticles at a distance of 20 nm from the point of photon absorption at t = 0.

This model does not predict the decay time that we observe in figure 4-7. The long decay time of several ns is due to the kinetic inductance of the SN-SPD as explained next.

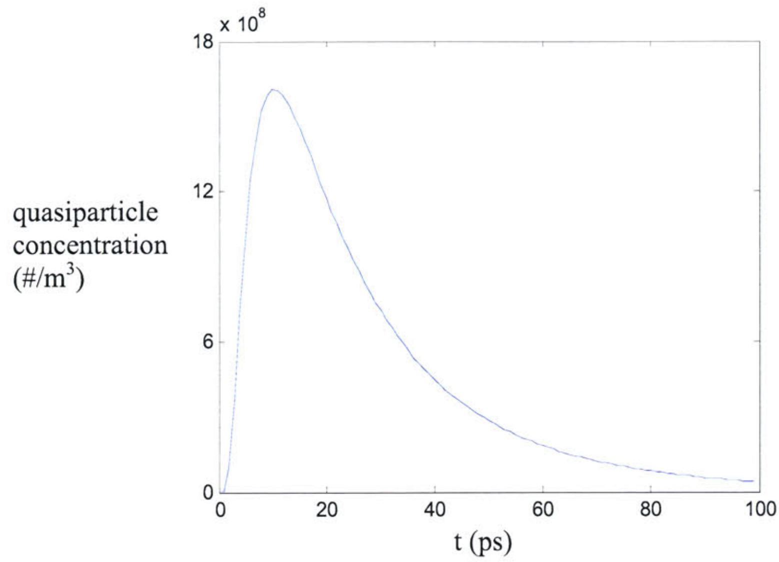


Figure 4-10: Matlab plot of quasiparticle concentration at a point 20 nm from photon absorption.

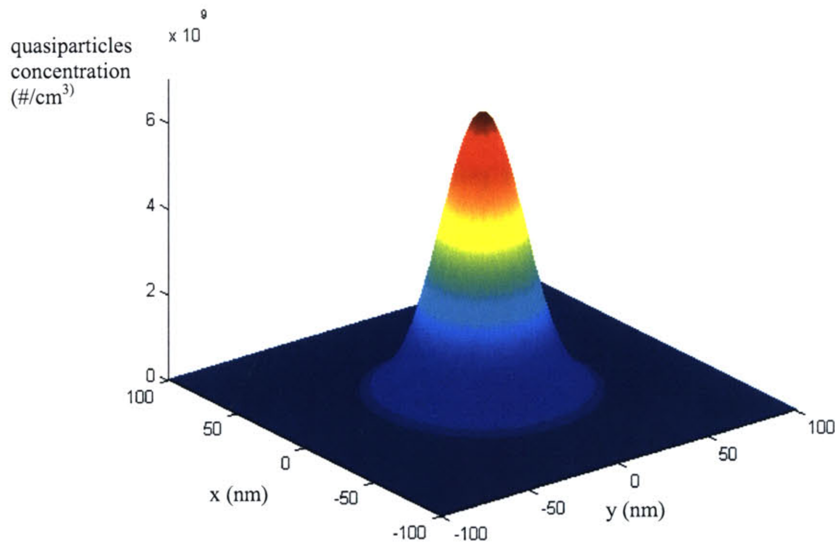


Figure 4-11: Matlab plot of quasiparticle concentration 4 ps after photon absorption. The hotspot size is in the order of several tens of nm.

### 4.4.2 Kinetic inductance of SN-SPD

The detector can be modeled as an inductor in series with a switch and a resistor in parallel. The kinetic inductance of a superconductor is due to the momentum of the cooper pairs. To change the direction of a steady state DC current is flowing

through a superconducting wire, force has to be applied to the cooper pairs to change its momentum. This leads to kinetic inductance in the superconducting wire. The kinetic inductance can be derived from the force, $F$, acting on a cooper pair as follows:

$$
\begin{aligned}
F &= \frac{\mathrm{d}}{\mathrm{d}t}(mv) && (4.29)\\
q\vec{E} &= \frac{\mathrm{d}}{\mathrm{d}t}(\frac{m}{nq}(nqv)) && (4.30)\\
\vec{E} &= \frac{\mathrm{d}}{\mathrm{d}t}(\frac{m}{nq^2}\vec{J}) && (4.31)
\end{aligned}
$$

where,

$$
\begin{aligned}
m &= 2m_e = \text{Cooper pair mass [kg]} && (4.32)\\
v &= \text{Cooper pair drift velocity [m/s]} && (4.33)\\
\vec{E} &= \text{Electric field [V/m]} && (4.34)\\
q &= 2e = \text{charge on a Cooper pair [C]} && (4.35)\\
n &= \text{Cooper pair density [\#/m}^3\text{]} && (4.36)\\
\vec{J} &= \text{current density [A/m}^2\text{]} && (4.37)
\end{aligned}
$$

Integrating equation (4.31) with respect to wire length, $l$, we obtain the voltage, $V$ across the wire.

$$
\begin{aligned}
V &= \frac{\mathrm{d}}{\mathrm{d}t}(\frac{ml}{Anq^2}\vec{J}A) = \frac{\mathrm{d}}{\mathrm{d}t}(LI) && (4.38)\\
L &= \frac{ml}{Anq^2} = \text{kinetic inductance [H]} && (4.39)\\
A &= \text{wire cross sectional area [m}^2\text{]} && (4.40)
\end{aligned}
$$

The detector can be modeled as shown in figure 4-12. In the absence of photons, the detector is simply the inductor, $L$, and the switch is closed to short out the detector normal-state resistance, $R_{\mathrm{n}}$. The entire bias current, $I_{\mathrm{b}}$, flows through the

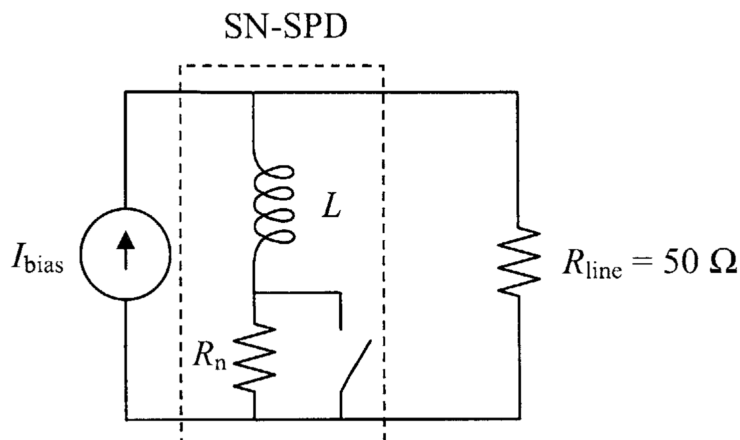


Figure 4-12: Schematic drawing showing an electrical model of the SN-SPD

device which shorts out the transmission-line input impedance, $R_{\text{line}}$. When a photon is absorbed, part of the nanowire goes normal for a very short period of time (on the time scale of the hotspot lifetime). This can be modeled as the opening and closing of the switch in figure 4-12. During the short period of time when the switch is open, the current through the device, $I_{\text{d}}$, drops according to the following equation:

$$I_{\text{d}} = \frac{R_{\text{n}}}{R_{\text{n}} + R_{\text{line}}} I_{\text{bias}} e^{-t\frac{R_{\text{n}}+R_{\text{line}}}{L}} + \frac{R_{\text{line}}}{R_{\text{n}} + R_{\text{line}}} I_{\text{bias}} \tag{4.41}$$

Say $I_{\text{d}} = I_{\text{close}}$ when the switch closes again, then the current through the device after the switch closes is:

$$I_{\text{d}} = (I_{\text{close}} - I_{\text{bias}}) e^{-t\frac{R_{\text{line}}}{L}} + I_{\text{bias}} \tag{4.42}$$

From equation (4.41) and (4.42) above, the rising edge of the voltage pulse has a time constant, $\tau_{\text{rise}} = \frac{L}{R_{\text{n}}+R_{\text{line}}}$ and the falling edge has a time constant, $\tau_{\text{fall}} = \frac{L}{R_{\text{line}}}$.

For a 6-$\mu$m-by-4-$\mu$m meander with 100-nm-wide wires in a 4-nm-thick film and $l$ = 120 $\mu$m, $L$ was measured to be $\sim$ 100 nH. Hence, $\tau_{\text{fall}} = 2$ ns which is close to the observed voltage pulse decay.

## 4.5 Future work

A method to increase the detection efficiency is to increase absorption of photons at the nanowires. We are currently developing an integrated optical resonator to reduce reflection off the detector surface thus increasing photon absorption.

We predict that narrower wires with dimensions approaching that of the hotspot will have higher detection efficiencies. In the extreme case where the wire width is less than or equal to the hotspot size, an absorbed photon will create a resistive barrier immediately without the need for current density to exceed $j_c$.

Although we have the fabrication capabilities to make wires as narrow as 25 nm, the signal to noise ratio of our high-speed setup is currently too low to test wires narrower than 75 nm. We plan to fabricate an on-chip readout circuitry to overcome this limitation. The on-chip circuitry will be a low-noise cryogenic amplifier of the device signal. This will enable the test of nanowire devices even narrower than 25 nm. It will also contribute to future efforts to build detector arrays.

We expect these improvements to have significant enabling impact on systems that use these devices.

# Bibliography

[1] A. Verevkin, A. Pearlman, W. Slysz, J. Zhang, M. Currie, A. Korneev, G. Chulkova, O. Okunev, P. Kouminov, K. Smirnov, B. Voronov, G. N. Gol'tsman, and R. Sobolewski. Ultrafast superconducting single-photon detectors for near-infrared-wavelength quantum communications. *Journal of Modern Optics*, 51(9-10):1447–1458, 2004.

[2] R. Pani, R. Pellegrini, M. N. Cinti, M. Mattioli, C. Trotta, L. Montani, G. Iurlaro, G. Trotta, L. D'Addio, S. Ridolfi, G. De Vincentis, and I. N. Weinberg. Recent advances and future perspectives of position sensitive PMT. *Nuclear Instruments & Methods in Physics Research Section B-Beam Interactions with Materials and Atoms*, 213:197–205, 2004.

[3] F. Zappa, S. Tisa, A. Gulinatti, A. Gallivanoni, and S. Cova. Complete single-photon counting and timing module in a microchip. *Optics Letters*, 30(11):1327–1329, 2005.

[4] S. Shiki, H. Sato, Y. Takizawa, T. Taino, C. Otani, and H. M. Shimizu. Detection of single optical photons with STJ detectors in RIKEN. *Nuclear Instruments & Methods in Physics Research Section a-Accelerators Spectrometers Detectors and Associated Equipment*, 520(1-3):530–532, 2004.

[5] D. Rosenberg, A. E. Lita, A. J. Miller, S. Nam, and R. E. Schwall. Performance of photon-number resolving transition-edge sensors with integrated 1550 nm resonant cavities. *IEEE Transactions on Applied Superconductivity*, 15(2):575–578, 2005.

[6] P. K. Day, H. G. LeDuc, B. A. Mazin, A. Vayonakis, and J. Zmuidzinas. A broadband superconducting detector suitable for use in large arrays. *Nature*, 425(6960):817–821, 2003.

[7] A. M. Kadin and M. W. Johnson. Nonequilibrium photon-induced hotspot: A new mechanism for photodetection in ultrathin metallic films. *Applied Physics Letters*, 69(25):3938–3940, 1996.

[8] G. Gol'tsman, O. Okunev, G. Chulkova, A. Lipatov, A. Dzardanov, K. Smirnov, A. Semenov, B. Voronov, C. Williams, and R. Sobolewski. Fabrication and properties of an ultrafast NbN hot-electron single-photon detector. *IEEE Transactions on Applied Superconductivity*, 11(1):574–577, 2001.

[9] G. Goltsman, A. Korneev, V. Izbenko, K. Smirnov, P. Kouminov, B. Voronov, N. Kaurova, A. Verevkin, J. Zhang, A. Pearlman, W. Slysz, and R. Sobolewski. Nano-structured superconducting single-photon detectors. *Nuclear Instruments & Methods in Physics Research Section a-Accelerators Spectrometers Detectors and Associated Equipment*, 520(1-3):527–529, 2004.

[10] A. Semenov, A. Engel, H.-W. Hubers, K. Il'in, and M. Siegel. Energy resolution of a superconductor quantum detector. *Proc. SPIE - Int. Soc. Opt. Eng. (USA)*, 5499(1):310–15, 2004.

[11] B. Berger. NASA To Test Laser Communications With Mars Spacecraft. *Space News Business Report*, Nov 15, 2004.

[12] G. Brassard and C. H. Bennett. Quantum cryptography. *Lecture Notes in Computer Science*, 325:79–90, 1988.

[13] F. Stellari and P. L. Song. Testing of ultra low voltage VLSI chips using the superconducting single-photon detector (SSPD). *Microelectronics Reliability*, 44(9-11):1663–1668, 2004.

[14] F. Stellari, P. L. Song, J. C. Tsang, M. K. McManus, and M. B. Ketchen. Testing and diagnostics of CMOS circuits using light emission from off-state leakage current. *IEEE Transactions on Electron Devices*, 51(9):1455–1462, 2004.

[15] G. N. Gol'tsman, O. Okunev, G. Chulkova, A. Lipatov, A. Semenov, K. Smirnov, B. Voronov, A. Dzardanov, C. Williams, and R. Sobolewski. Picosecond superconducting single-photon optical detector. *Applied Physics Letters*, 79(6):705–707, 2001.

[16] A. D. Semenov, G. N. Gol'tsman, and A. A. Korneev. Quantum detection by current carrying superconducting film. *Physica C*, 351(4):349–356, 2001.

[17] Joel K.W. Yang, E. Dauler, A. Ferri, A. Pearlman, A. Verevkin, G. Goltsman, B. Voronov, R. Sobolewski, W.E. Keicher, and K.K. Berggren. Fabrication development for nanowire GHz-counting-rate, single photon detectors. *IEEE Transactions on Applied Superconductivity*, 15(2):626–630, 2005.

[18] M. J. Word, I. Adesida, and P. R. Berger. Nanometer-period gratings in hydrogen silsesquioxane fabricated by electron beam lithography. *Journal of Vacuum Science & Technology B*, 21(6):L12–L15, 2003.

[19] H. Namatsu, Y. Takahashi, K. Yamazaki, T. Yamaguchi, M. Nagase, and K. Kurihara. Three-dimensional siloxane resist for the formation of nanopatterns with minimum linewidth fluctuations. *Journal of Vacuum Science & Technology B*, 16(1):69–76, 1998.

[20] D. Gil, R. Menon, and H. I. Smith. Fabrication of high-numerical-aperture phase zone plates with a single lithography exposure and no etching. *Journal of Vacuum Science & Technology B*, 21(6):2956–2960, 2003.

[21] M. Hatzakis, B. J. Canavello, and J. M. Shaw. Single-step optical lift-off process. *IBM Journal of Research and Development*, 24(4):452–460, 1980.

[22] J. G. Goodberlet, J. T. Hastings, and H. I. Smith. Performance of the Raith 150 electron-beam lithography system. *Journal of Vacuum Science & Technology B*, 19(6):2499–2503, 2001.

[23] T. H. P. Chang. Proximity effect in electron-beam lithography. *Journal of Vacuum Science & Technology*, 12(6):1271–1275, 1975.

[24] E. H. Anderson, D. L. Olynick, W. L. Chao, B. Harteneck, and E. Veklerov. Influence of sub-100 nm scattering on high-energy electron beam lithography. *Journal of Vacuum Science & Technology B*, 19(6):2504–2507, 2001.

[25] S. A. Rishton and D. P. Kern. Point exposure distribution measurements for proximity correction in electron-beam lithography on a sub-100 nm scale. *Journal of Vacuum Science & Technology B*, 5(1):135–141, 1987.

[26] G. P. Watson, L. A. Fetter, and J. A. Liddle. Dose modification proximity effect correction scheme with inherent forward scattering corrections. *Journal of Vacuum Science & Technology B*, 15(6):2309–2312, 1997.

[27] K. Takahashi, M. Osawa, M. Sato, H. Arimoto, K. Ogino, H. Hoshino, and Y. Machida. Proximity effect correction using pattern shape modification and area density map. *Journal of Vacuum Science & Technology B*, 18(6):3150–3157, 2000.

[28] C. L. Frye and W. T. Collins. Oligomeric silsesquioxanes, (hsio3/2)n. *J. Am. Chem. Soc.*, 92(19):5586–5588, 1970.

[29] J. H. Zhao, I. Malik, T. Ryan, E. T. Ogawa, P. S. Ho, W. Y. Shih, A. J. McKerrow, and K. J. Taylor. Thermomechanical properties and moisture uptake characteristics of hydrogen silsesquioxane submicron films. *Applied Physics Letters*, 74(7):944–946, 1999.

[30] M. J. Loboda, C. M. Grove, and R. F. Schneider. Properties of a-siox: H thin films deposited from hydrogen silsesquioxane resins. *Journal of the Electrochemical Society*, 145(8):2861–2866, 1998.

[31] F. C. M. J. M. van Delft. Delay-time and aging effects on contrast and sensitivity of hydrogen silsesquioxane. *Journal of Vacuum Science & Technology B*, 20(6):2932–2936, 2002.

[32] W. Henschel, Y. M. Georgiev, and H. Kurz. Study of a high contrast process for hydrogen silsesquioxane as a negative tone electron beam resist. *Journal of Vacuum Science & Technology B*, 21(5):2018–2025, 2003.

[33] T. Nakamura, M. Sasaki, A. Kobayashi, K. Sawa, and K. Mine. Oxidative curing of hydrogen silsesquioxane resin films by electron beam irradiation without additional heatings and characterization of the cured films. *Japanese Journal of Applied Physics Part 1-Regular Papers Short Notes & Review Papers*, 40(11):6187–6191, 2001.

[34] M. Peuker, M. H. Lim, H. I. Smith, R. Morton, A. K. van Langen-Suurling, J. Romijn, E. W. J. M. van der Drift, and F. C. M. J. M. van Delft. Hydrogen silsesquioxane, a high-resolution negative tone e-beam resist, investigated for its applicability in photon-based lithographies. *Microelectronic Engineering*, 61-2:803–809, 2002.

[35] Charles P. Poole, Horacio A. Farach, and Richard J. Creswick. *Superconductivity*. Academic Press, San Diego, 1995.